NASA/TM-20260000217

Characterization of Lunar Simulant Deposition on Seals for Lunar Surface Applications

Jackson Stewart and Patrick H. Dunlap, Jr.
Glenn Research Center, Cleveland, Ohio

February 2026

NASA STI Program Report Series

Since its founding, NASA has been dedicated to the advancement of aeronautics and space science. The NASA scientific and technical information (STI) program plays a key part in helping NASA maintain this important role.

The NASA STI program operates under the auspices of the Agency Chief Information Officer. It collects, organizes, provides for archiving, and disseminates NASA's STI. The NASA STI program provides access to the NTRS Registered and its public interface, the NASA Technical Reports Server, thus providing one of the largest collections of aeronautical and space science STI in the world. Results are published in both non-NASA channels and by NASA in the NASA STI Report Series, which includes the following report types:

- TECHNICAL PUBLICATION.
  Reports of completed research or a major significant phase of research that present the results of NASA programs and include extensive data or theoretical analysis. Includes compilations of significant scientific and technical data and information deemed to be of continuing reference value. NASA counterpart of peer-reviewed formal professional papers but has less stringent limitations on manuscript length and extent of graphic presentations.

- TECHNICAL MEMORANDUM.
  Scientific and technical findings that are preliminary or of specialized interest, e.g., quick release reports, working papers, and bibliographies that contain minimal annotation. Does not contain extensive analysis.

- CONTRACTOR REPORT.
  Scientific and technical findings by NASA-sponsored contractors and grantees.

- CONFERENCE PUBLICATION.
  Collected papers from scientific and technical conferences, symposia, seminars, or other meetings sponsored or cosponsored by NASA.

- SPECIAL PUBLICATION.
  Scientific, technical, or historical information from NASA programs, projects, and missions, often concerned with subjects having substantial public interest.

- TECHNICAL TRANSLATION.
  English-language translations of foreign scientific and technical material pertinent to NASA's mission.

Specialized services also include organizing and publishing research results, distributing specialized research announcements and feeds, providing information desk and personal search support, and enabling data exchange services.

For more information about the NASA STI program, see the following:

- Access the NASA STI program home page at http://www.sti.nasa.gov

NASA/TM-20260000217

Characterization of Lunar Simulant Deposition on Seals for Lunar Surface Applications

Jackson Stewart and Patrick H. Dunlap, Jr.
Glenn Research Center, Cleveland, Ohio

National Aeronautics and
Space Administration

Glenn Research Center
Cleveland, Ohio 44135

February 2026

Acknowledgments

The authors would like to acknowledge NASA's Human Landing System (HLS) Program for supporting this effort. They would also like to thank Annabelle Hegeman, Janice Mather, and Nathan Jimenez for their technical contributions to this work.

Trade names and trademarks are used in this report for identification only. Their usage does not constitute an official endorsement, either expressed or implied, by the National Aeronautics and Space Administration.

Level of Review: This material has been technically reviewed by technical management.

This report is available in electronic form at https://www.sti.nasa.gov/ and https://ntrs.nasa.gov/

NASA STI Program/Mail Stop 050
NASA Langley Research Center
Hampton, VA 23681-2199

Contents

Characterization of Lunar Simulant Deposition on Seals for Lunar Surface Applications

Jackson Stewart and Patrick H. Dunlap, Jr.
National Aeronautics and Space Administration
Glenn Research Center
Cleveland Ohio 44135

Abstract

Since its development at NASA Glenn Research Center (GRC) in 2020, the Uniform Dust Deposition System (UDDS) has been used to evenly deposit precise amounts of lunar regolith simulant onto a wide range of materials and test articles. Equally important to the uniformity of and control over the simulant deposition is the ability to accurately quantify the amount of simulant deposited. This paper outlines the method that has been developed to make these deposition level measurements and relevant considerations when adapting this method for other similar applications. An overview of the equipment used is provided, highlighting key specifications. The benefits and drawbacks of a range of potential image processing techniques are described, justifying panoptic segmentation as the most insightful approach for characterizing dust deposited on a surface. The importance of applying basic sampling statistics is emphasized to allow the generation of confidence intervals about various measures of dust deposition level. All prior considerations are integrated in an overview of the current image processing methodology used with the UDDS to characterize lunar simulant deposited on the surface of elastomer seals, as an example. Lastly, a few emerging areas of interest are described and contextualized: correlating image-based measures of deposition level with mass-based approaches and using image data to generate alternative predictors of performance that incorporate underlying physics specific to the test article.

Uniform Dust Deposition System Overview

Hardware Configuration

The Uniform Dust Deposition System (UDDS) was developed at the NASA Glenn Research Center to provide repeatable, uniform, and automated deposition of lunar regolith simulants on surfaces of interest for dust mitigation testing. Although this system was originally developed to help test seals for future lunar surface systems, it has also been used to test other mechanical components and remains mostly unaltered from the configuration first described by Gerdts et al. in NASA/TM-20210024128 (Ref. 1). The UDDS consists of three primary subsystems: the regolith simulant (which will be referred to interchangeably as ‘dust’) deposition subsystem, the transfer subsystem, and the imaging subsystem. These three subsystems are all housed within a humidity-controlled (<0.5% RH) glove box equipped with HEPA filtration to contain any airborne dust. NASA/TM-20210024128 also outlines the simulant preparation procedures used for dust depositions. This system and the associated procedures were used to generate all data presented in this body of work.

Imaging Equipment and Specifications

Because the imaging systems and subsequent image processing methods are the primary focus of this work, the equipment used to capture these images is outlined below. The UDDS workflow involves two imaging setups: the original imaging subsystem installed inside the glovebox which uses a

stereomicroscope and camera to inspect the sample surfaces, and an auxiliary light box which was set up more recently and uses a digital single-lens reflex (DSLR) camera with a macro lens.

The ‘micro’ setup captures images with a resolution of 3664 x 2748 pixels and a field of view of roughly 2.45 x 1.84 mm (with a resolution of 0.000670 mm/px). These images are used in the analysis to characterize a dust deposition. A Motic SMZ-171 Trinocular Head microscope is used, which has been modified with a motorized focus stage for more convenient control that has been integrated into the UDDS electronics. A Motic 10.0MP USB camera has been installed on the microscope with a 0.5X C-mount adapter to capture images.

The ‘macro’ setup captures images with a resolution of 5472 x 3648 pixels and a field of view of roughly 33 x 22 mm (with a resolution of 0.00602 mm/px). These images collectively document the state of the entire seal surface. This setup is installed inside a photography LED light box made by Fotodiox. An aluminum extrusion frame was constructed to suspend a Canon EOS 70D camera with a Canon 60mm f/2.8 Macro USM lens above the test article, which is loaded into the light box and onto a graduated rotating fixture to allow precise and repeatable positioning of the test article underneath the camera.

Macroscopic Versus Microscopic Images

Both image types—macroscopic and microscopic, as outlined previously—offer benefits and drawbacks when aiming to characterize a dust deposition. Macro images capture a greater portion of the seal surface and thus provide a more comprehensive representation of a deposition at a magnification level that is intuitive to interpret. However, this scale comes with an inherently lower resolution than micro images, with the pixel density of macro images being an order of magnitude above that of the UDDS micro image setup. An example macro image is shown in Figure 1.

Because of the significantly higher magnification, micro images capture a much more limited portion of the seal surface than a macroscopic image. This limited field of view comes with the risk of poorly representing the entire seal surface, especially if there is limited confidence in the spatial uniformity of a deposition. As will be discussed in greater detail in the ‘Sampling Statistics Considerations’ section, this shortfall can be overcome by integrating some basic sampling statistics into the analysis. An example of a micro image of the same seal and dust deposition as Figure 1 is shown below in Figure 2.

Figure 1.—Macroscopic image of dust on a NASA Docking System (NDS) seal post-deposition.

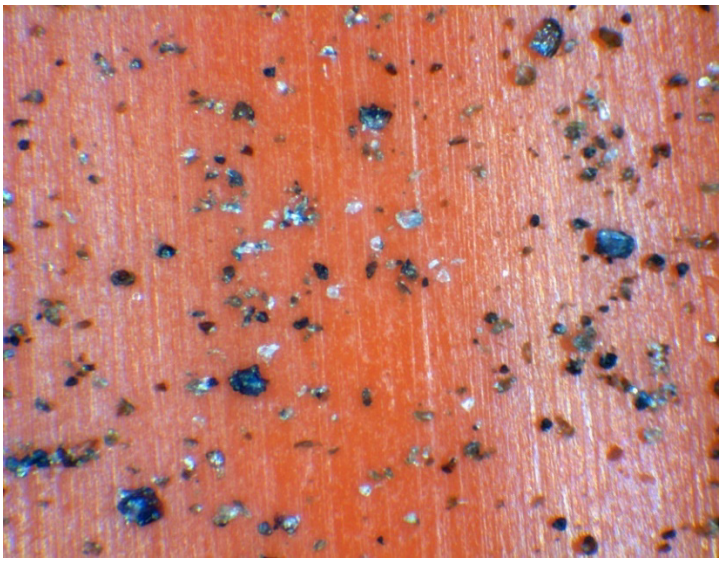

Figure 2.—Microscopic image of the same NDS seal shown in Figure 1 after dust deposition.

The NDS seal shown in Figure 1 and Figure 2 is a subscale version of the full-scale seal with the same cross section but a reduced diameter of only 27.6 cm. Typically for test seals of this size, 36 equally spaced macro images are captured of the sealing surface. The 10° offset of each image paired with the camera field of view allows slight overlap between consecutive images and as a result collectively captures the entire seal surface. For a similarly sized seal, only eight micro images are typically taken of the seal surface, equally spaced 45° apart along the circumference of the seal. This has been found to be an acceptable sample size to verify the uniformity of the dust deposition and reduce uncertainty resulting from limited sampling (see 'Choosing Number of Images' for more information).

Parameters of Interest

Percent Area Coverage

Most image-based dust deposition characterization methods utilized to-date employ a metric called Percent Area Coverage (PAC), which is the percentage of the 2D image plane occupied by particles:

$$PAC = 100 \times \left(\frac{n_{particle}}{n_{particle} + n_{background}} \right) \tag{1}$$

Where n is the number of pixels belonging to either the particle or background class. For the panoptic segmentation algorithm described previously where the pixels within each particle are given a unique identifier, $n_{particle}$ is determined by counting the number of pixels belonging to all identifier classes except those denoting the background.

Dust Mass Surface Density

An alternative dust deposition characterization approach is to measure the mass of deposited dust and divide that by the surface area over which the dust was deposited. This results in a parameter called the Dust Mass Surface Density (σ_{dust}), defined as

$$\sigma_{dust} = \frac{m_{dust}}{A} \tag{2}$$

where m_{dust} is the mass of deposited regolith (in grams) and A is the surface area over which the dust is deposited (in cm^2). Because the amount of dust deposited on a test article is often quite small (e.g., on the order of 10^{-3} g), it can be difficult to accurately measure the mass of deposited dust on large, heavy test articles. Methods have been developed such as those outlined in NASA-STD-1008 Section 5.2.1.1.d which use lighter witness samples placed over portions of the test hardware. However, this approach comes with the inherent tradeoff that portions of the test article surface could be covered by witness samples and thus would receive no dust deposition.

Overview of Segmentation Methods

Once macro and micro images are captured for a given dust deposition, they must be processed to characterize the amount of dust deposited. The first step in this process is segmentation: classifying each pixel within the image as belonging to either a dust particle or the elastomer seal background. An abundance of information is available in the literature about the types of segmentation—this section discusses the implications of the three most relevant types within a dust deposition context (Ref. 2).

Semantic, Instance, and Panoptic Segmentation

Semantic segmentation seeks to assign each pixel a class label based on the object(s) being detected. For an image such as Figure 2, there are two classes: background and simulant. This kind of segmentation does not differentiate between two objects within the same class, however, meaning that there is no identification of distinct particles, but rather whether a given pixel belongs to *any* particle or the background. A simple color thresholding approach would achieve this type of segmentation, although the state of the art is defined by machine learning techniques. Because each pixel receives a class label, calculating the PAC is as simple as counting the number of pixels labelled ‘particle’ relative to the number labelled ‘background.’ However, this kind of segmentation would not be able to return the particle count for an image because of the lack of differentiation between distinct particles.

Inversely, instance segmentation seeks to identify individual occurrences of a given object within an image. If given an image like Figure 2 and trained to detect particles, for example, an instance segmentation algorithm would be able to report the number of particles present and draw a unique bounding box around each one. The output would not, however, be able to provide the total number of pixels that belong to the simulant or background, preventing a PAC calculation.

Panoptic segmentation combines features of the prior two approaches, enabling both pixel-level classification and individual instance detection. Using this method, each pixel in an image receives both a class label and a unique instance identifier. For example, pixels belonging to two different particles would both belong to the ‘particle’ class but would receive unique identifies such as ‘particle 1’ and ‘particle 2.’ This approach allows for PAC calculations as well as other insights discussed in later sections. This type of classification is commonly achieved with machine learning techniques, but an alternative image processing workflow is presented in this paper using a series of image transformations instead.

Thresholding Versus Image Processing Versus Machine Learning

There are several viable approaches to segment an image to measure the level of dust deposition on a surface. The simplest is thresholding. If the background surface has a distinct color such as the bright orange elastomer of the NDS seal shown in Figure 2, it could be assumed that all pixels that are significantly different than the background are particles. One method to employ this approach would be to take an image of a pristine seal like the NDS seal shown to the left in Figure 3, then convert the image

from a Red-Green-Blue (RGB) color scheme to Hue-Saturation-Value (HSV). Then, isolate the Hue channel and note the range of values present, as shown below in Figure 3.

Then, after depositing dust, all pixels whose hue is outside the bounds identified previously could be considered particles and counted as such for a PAC calculation. Figure 4 depicts the impact the presence of dust has on the HSV histogram for the image, which clearly shows additional hues present outside the nominal background hue range. This technique is computationally inexpensive and straightforward to implement but is limited by the restrictions of semantic segmentation discussed previously.

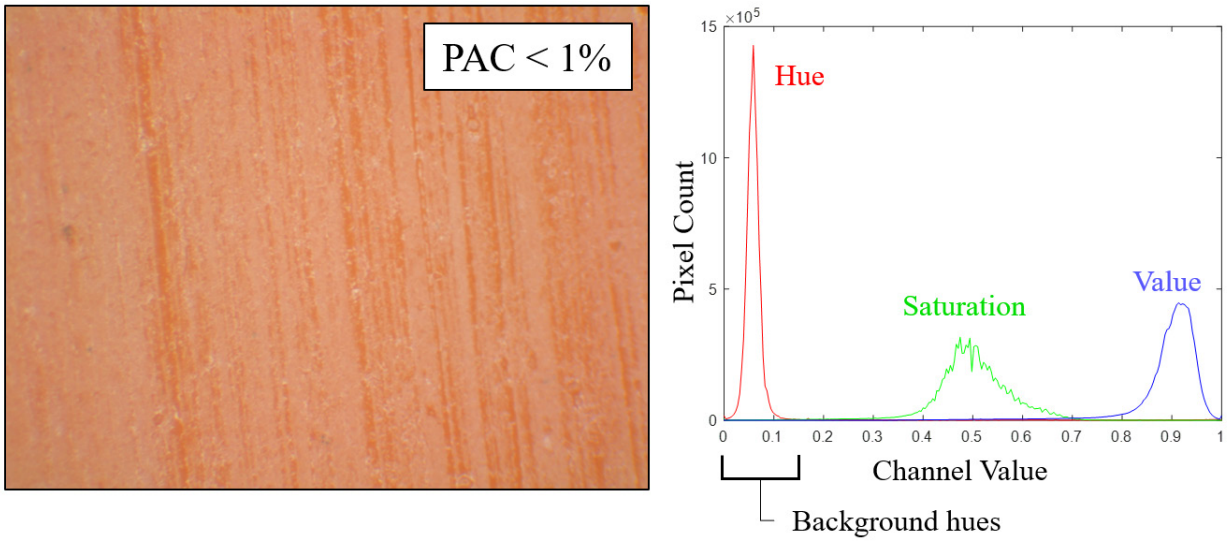

Figure 3.—Pristine seal HSV histogram.

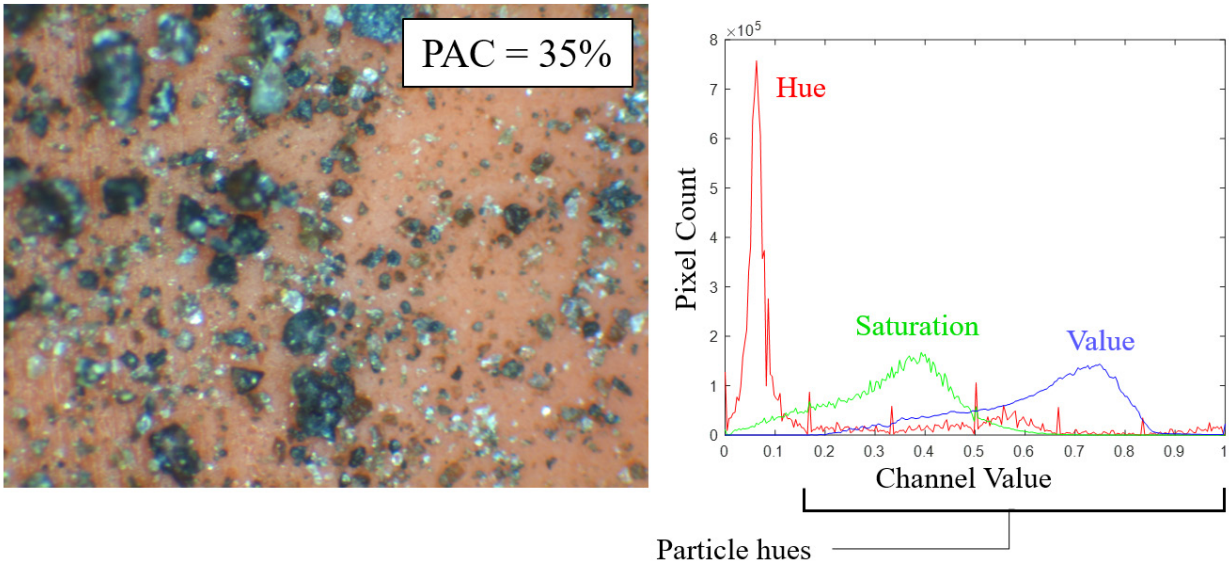

Figure 4.—Dust-covered seal HSV histogram.

Image processing techniques beyond simple thresholding offer additional insight at the cost of complexity and compute time. A series of image transformations such as those outlined in the ‘Current Image Processing Methods’ section could be employed to enable the benefits of panoptic segmentation without the tedium of manually labelling training data for a machine learning approach. The literature contains many examples of image processing techniques developed in the medical microscopy field for identifying and characterizing features like cells and cell nuclei which can be adapted to work with particles against a uniform background surface (Ref. 3).

Alternatively, a machine learning approach can be taken to identify particles. There is also significant literature available outlining the setup and use of neural networks for all types of segmentation (Ref. 4). Neural networks can be quite accurate but are limited by the quality of the training dataset used. Even transfer learning models require manually labelled training data, where a user must outline each particle in many images by hand. Jimenez trained a model using the open-source software ImageJ to perform semantic segmentation of particles on an elastomer seal, whose output is a probability map of the image where each pixel’s value is the probability it contains a particle (Ref. 5). This probability map is then thresholded (i.e., to ensure at least 95% confidence that a pixel contains a particle), and the result can be used to perform a PAC calculation as demonstrated in Figure 5. However, additional image processing techniques must still be performed on this output binary mask to achieve panoptic segmentation for insight beyond simple PAC estimation. To avoid this additional step, a panoptic segmentation model would need to be trained with significantly more training data.

The image analysis technique used to analyze data should be selected based on the application, available resources, and desired accuracy. If a quick and simple PAC measurement is needed, thresholding might be sufficient (refer to the ‘Sampling Statistics Considerations’ section concerning the accuracy of this approach, depending on input image resolution). If information is required about individual particle size, particle size distribution, or dust mass surface density, then more sophisticated image processing or machine learning techniques will be required that are capable of panoptic segmentation.

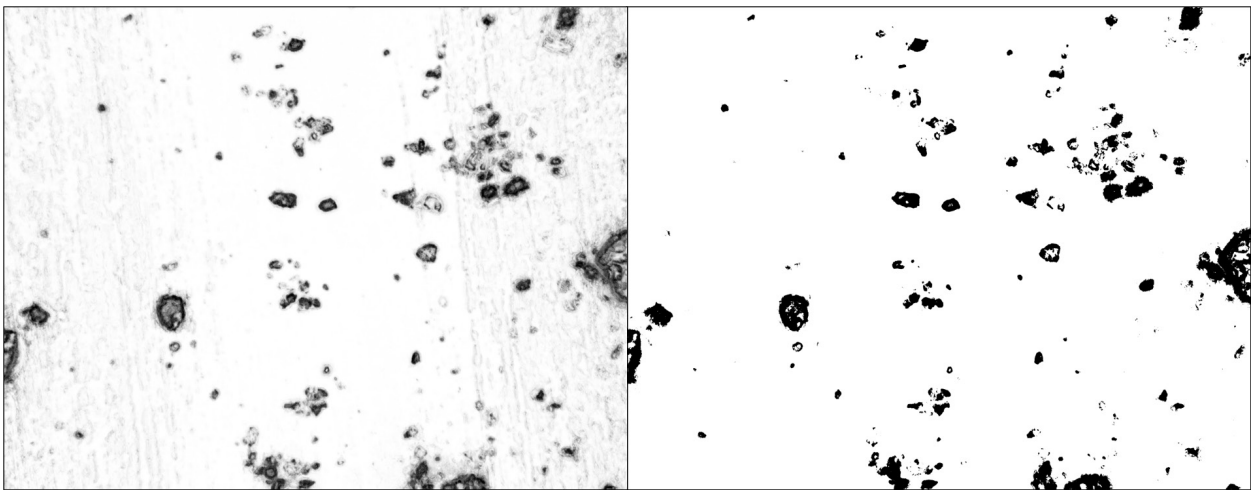

Figure 5.—Neural-net-generated probability map (left) and resulting binary mask after thresholding (right).

Sampling Statistics Considerations

Choosing Number of Images

The standard deviation of the deposition over a seal surface has been demonstrated to be less than 0.25 mg/cm^2 using the UDDS and its standard operating procedures (Ref. 1). For the purposes of analysis, it can be assumed that the deposition level is uniform across the seal surface, and that sample measurements taken of the deposition level will be normally distributed.

Historically, eight equally spaced microscope images were taken along the circumference of a test seal. Each image underwent the analyses outlined in the 'Current Image Processing Methods' section of this paper, resulting in eight PAC and eight σ_{dust} measurements for a given deposition. The sample mean of each metric was calculated. To generate a 95% confidence interval for both the PAC and σ_{dust} estimates, the sample standard deviation formula shown in Equation (3) was used.

$$s = \sqrt{\frac{\sum_{i=1}^{n}(x_i - \bar{x})^2}{n-1}} \tag{3}$$

where s is the sample standard deviation, n is the number of samples (typically eight images), x_i is either the PAC or σ_{dust} measurement for the i^{th} sample image, and $\bar{x}$ is the sample mean PAC or σ_{dust}. The sample standard deviation s is then multiplied by two before adding and subtracting from the sample mean to yield 95% confidence intervals for either the PAC or σ_{dust} of a deposition. This same calculation was performed for macroscopic images such as the one shown in Figure 1, which were analyzed using a color thresholding technique similar to what Hurlbert et al. outlined in 2023(Ref. 6).

A total of 36 macro images were taken per deposition, collectively capturing the entire seal surface. Twenty-eight depositions were performed where both micro and macro images were used to measure the PAC of each deposition and compare the results of micro versus macro imaging approaches. The resulting PAC estimates for all depositions are shown in Figure 6 using both techniques. Individual deposition confidence intervals are not the focus of the figure, but rather the general shape of the intervals collectively. Note that, especially for deposition levels at or above around 20 PAC, the macro image approach generates much wider confidence intervals. This is likely because of the inherently lower spatial resolution of the images collected at the macro scale. With increasing particle density on the surface, color thresholding approaches struggle to differentiate between particle and background because the two effectively get combined and averaged within a single pixel. The confidence intervals for the micro images appear less impacted by increasing PAC, since the higher resolution means that the analysis can resolve the space between particles even as the distance between them decreases.

It is also worth noting that the standard deviation in PAC measurements for a given deposition was usually higher for the macro image analysis than for the analysis of the micro images, despite the sample size being over four times as large for this method. It can be concluded that the accuracy of the image analysis is lower for macro than micro images because it results in wider confidence intervals despite benefitting from a higher sample size.

Similarly, it is worth investigating if eight micro images per deposition is sufficient to accurately and confidently characterize the deposition level. The same 28-deposition dataset depicted in Figure 6 can be used to change the number of micro images used for analysis and monitor impacts on PAC measurement uncertainty. While additional micro images cannot retroactively be captured for past depositions to increase the sample size above 8 measurements per deposition, the existing sample size of eight can be artificially and randomly reduced as if fewer images had been taken. Figure 7 displays this approach applied to each of the 28 depositions, ranging from a sample size of four up to the original eight images.

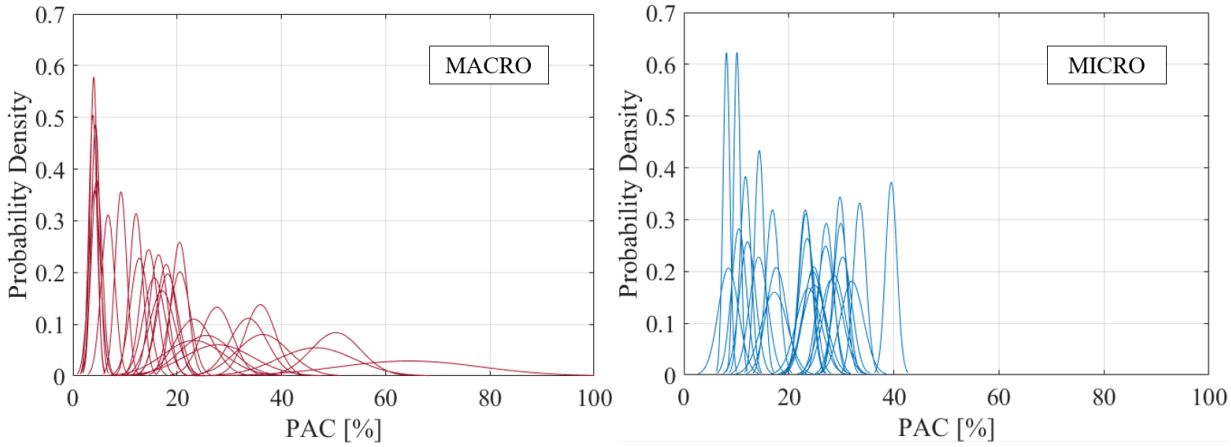

Figure 6.—Uncertainty in deposition level based on macro (left) and micro (right) images.

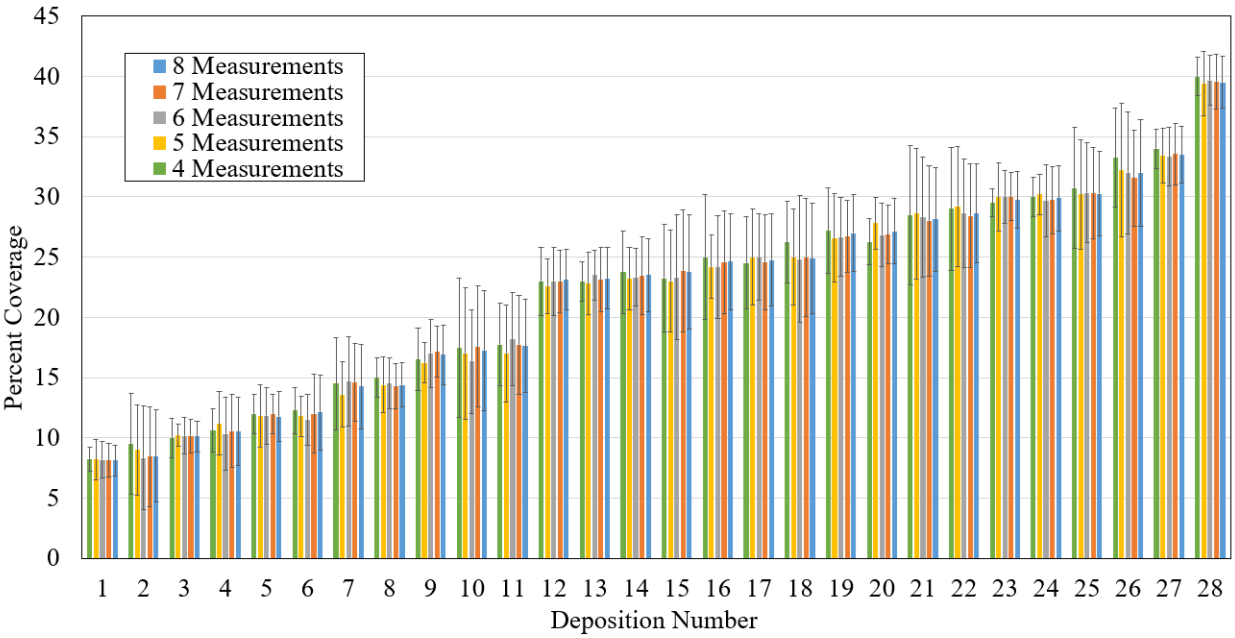

Figure 7.—Image count impact on confidence interval.

Note that the 95% confidence interval generally appears to narrow with increases in sample size for a given deposition. This result is expected, but the strength of the correlation is minor relative to the total uncertainty present. Critical and precise deposition characterizations may justify increasing the number of micro images taken to lower uncertainty. This increased measurement confidence must be balanced with the additional time required to collect and analyze additional image samples.

Methods for Quantifying Segmentation Error

A segmentation method has limited technical value without a means to monitor its accuracy. With machine learning approaches, this is achieved by partitioning data into training, test, and validation sets. With image processing approaches such as the one outlined in this report, the task of validation becomes more open ended. Nonetheless, a best effort should be made to ensure the PAC and σ_{dust} measurements are reliable by attempting to quantify their accuracy. This becomes a difficult task, especially if trying to avoid the tedium of hand labelling validation images. An alternative approach was developed that aims to

validate the accuracy of the segmentation algorithm without having to compare to hand labelled images. This approach also eliminates all human error that results from labelling particle outlines by hand.

A Matlab script was written that simulates the deposition process and generates a simplified image of a seal surface contaminated by a known quantity of dust. The user inputs a desired PAC value, and the script will simulate adding dust particles to the surface until the desired PAC value is reached. Particles are approximated as circles whose center location is sampled from a uniform spatial distribution, while the diameter is sampled from a specified particle size distribution (PSD) (for this analysis, the PSD of lunar regolith simulant JSC-1A was used to allow comparison to test data collected with this simulant). The intent with this approach is that, because the deposition is simulated, the resulting image has a 'true PAC' value that is known exactly without the need to hand label.

Another benefit of this approach is that it allows for the parameterization of image resolution. The microscopy setup used to collect images has a pixel width of 0.00067 mm, which is below even the ~0.001 mm diameter Q_{99} fines of JSC-1A simulant (the diameter that is smaller than 99% of particles in a simulant) and roughly an order of magnitude below the grain sizes measured from Apollo 11, 12, 14, and 15 samples (Ref. 7). Being able to assess the accuracy of the segmentation algorithm over a wide range of image resolutions will inform if additional image resolution is needed to accurately measure PAC and σ_{dust}. Three image resolutions were assessed: 1/10000 mm/px, 1/1000 mm/px, and 1/100 mm/px (for reference, the UDDS microscope setup has a resolution of 1/1493 mm/px). The intent behind selecting these three resolutions for comparison was to capture a wide range, both above and below the currently implemented resolution. An example of each resolution is shown in Figure 8. For reference, a sample image with 1/10 mm/px is also included to demonstrate the importance of ensuring that the imaging system used has a resolution sufficiently high to resolve individual particles. The field of view for each image is the same as that of the UDDS microscope, with image dimensions provided in Table 1.

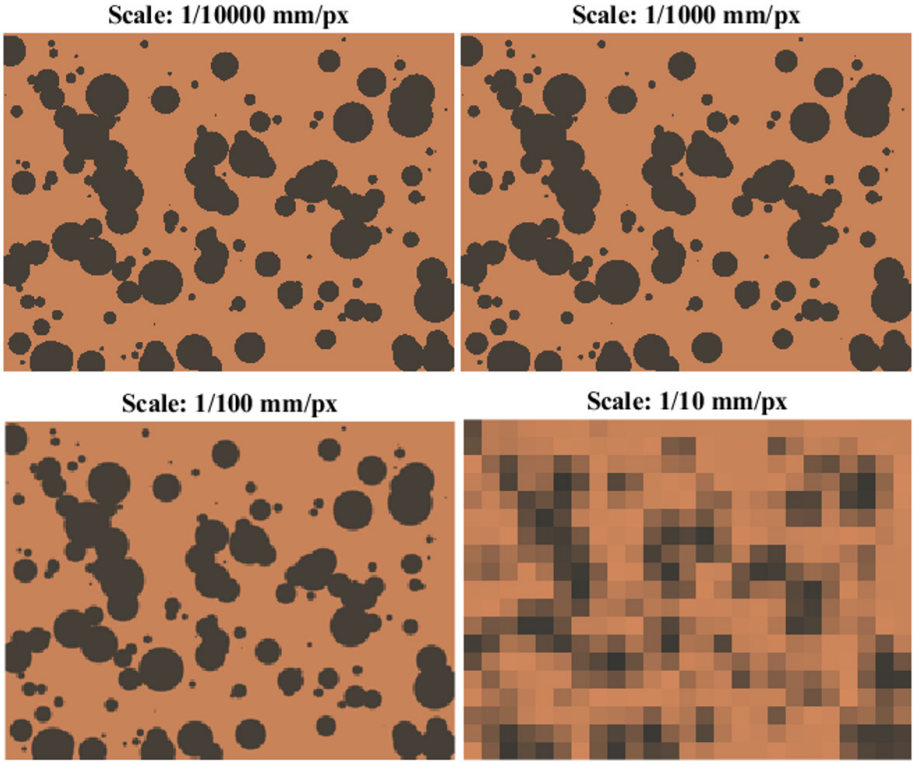

Figure 8.—Comparison of image resolutions displaying simulated JSC-1A deposition.

A total of 40 simulated depositions were completed for each of the three resolutions using a ‘virtual’ JSC-1A simulant. Particle diameters were selected according to the PSD of JSC-1A available in the literature (Ref. 8). Depositions were simulated at 5% PAC increments from 5% up to 50%, with a total of four depositions completed at each deposition level. The ‘true’ PAC was recorded for each deposition, which is the actual PAC value at which the simulation stopped the deposition. Because the process was simulated, this value was known with absolute certainty. The resulting simulated images were fed into the image segmentation algorithm outlined in this report, and the resulting ‘measured’ PAC was compared to the true/nominal value for each image. These comparisons are summarized in Figure 9 for each of the three image resolutions simulated.

TABLE 1.—SIMULATED DEPOSITION IMAGE SPECIFICATIONS

Pixel width [mm/px]	Image dimensions [px]	Field of view [mm]
1/10000	24541 x 18406	2.455 x 1.841
[1]1/1493	3664 x 2748	
1/1000	2455 x 1841	
[2]1/166	5472 x 1201	32.94 x 7.23
1/100	246 x 185	2.455 x 1.841
1/10	25 x 19	

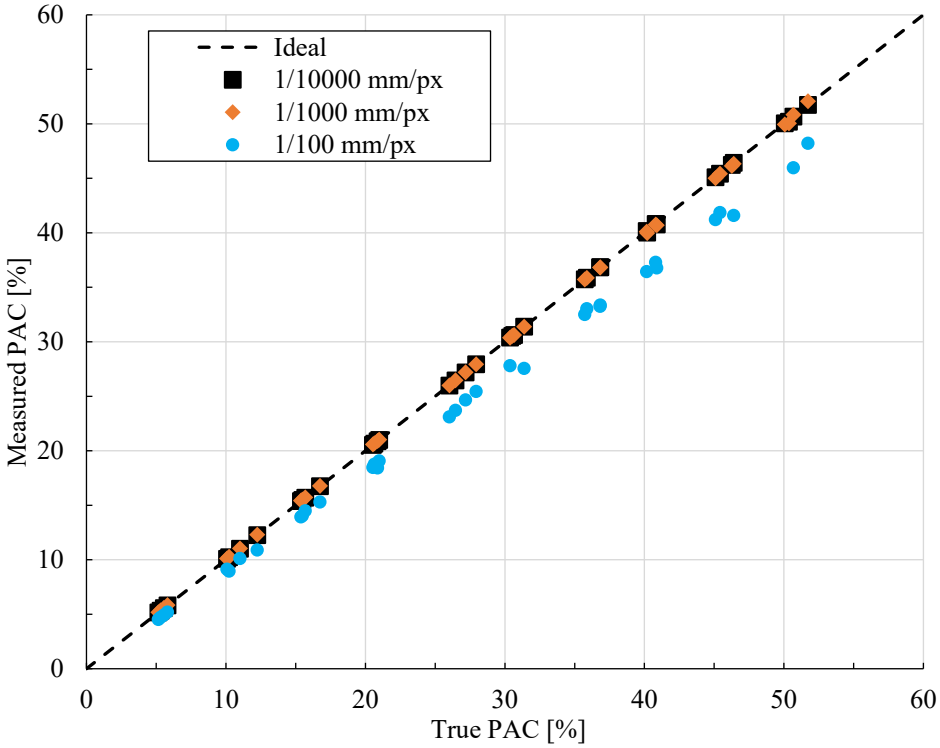

Figure 9.—Comparison of true PAC with results of image segmentation algorithm.

[1] UDDS microscopy image specifications, for reference
[2] Macro image specifications, for reference

Note that while the lowest resolution (largest mm/px value) images display some deviation from an accurate PAC measurement, both 1/1000 and 1/10000 mm/px images yield practically identical results. This supports the conclusion that there is insignificant additional accuracy to be gained from further increasing the image resolution of the current UDDS microscopy setup. However, trying to segment images using images with worse than 1/1000 mm/px spatial resolutions may begin to introduce error into PAC measurements and all subsequent calculations. This finding advocates against the use of something like a standard macro imaging setup using a DSLR camera with a macro lens for precise PAC determination (Even with a high-end macro lens, the macro image setup described previously was measured to have a pixel width of 1/166 mm/px). The implications of this result are further compounded by the wider confidence intervals associated with lower image resolutions shown previously in Figure 6. To quantify the difference between true and measured PAC values, the percent error (PE) was calculated for each datapoint using Equation (4)

$$PE = 100 * \left| \frac{PAC_M - PAC_T}{PAC_T} \right| \tag{4}$$

where PAC_M is the measured PAC and PAC_T is the true PAC of a given image. The PE is plotted against each simulated true PAC value in Figure 10.

A similar trend emerges from Figure 10 as did with Figure 9: there is little difference between the two finer resolutions, while the 1/100 mm/px resolution exhibits distinctly higher error. While the simulated images used here are undoubtedly a best-case scenario from an image processing standpoint, they demonstrate that the segmentation approach can be implemented successfully with minimal error. In practice, additional margins should be added to account for imperfect image focus, sensor noise, and other discrepancies between simulated and real deposition images. The PE values shown in Figure 10 serve as a lower limit to what could be reasonably expected when analyzing real images taken from the UDDS. At the very least, this analysis demonstrates that the UDDS has sufficient resolution to detect the entire practical range of JSC-1A simulant without having to manually label all particles across several validation images.

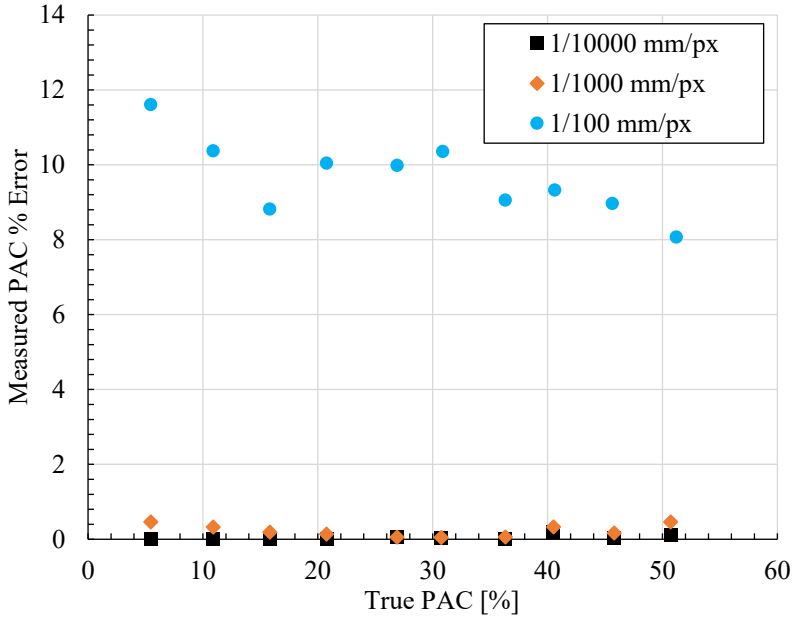

Figure 10.—Percent error in PAC measurements.

Current Image Processing Methods

Calibration of Pixel Width

Careful calibration of the UDDS imaging system is critical for the accurate conversion of lengths measured in pixels to millimeters. To perform this calibration, a precision graduated scale was placed under the microscope, and images were taken with the rule horizontally and vertically oriented. The finest markings on this scale were 1/64 in. apart. Each image was loaded into Matlab's Image Viewer application, which allows precise length measurements to be taken (measured in pixels). The center-to-center distance between adjacent 1/64-in. graduations was measured and recorded multiple times spanning the entire width and height of the image to mitigate the impacts of perspective distortion. A total of 30 measurements were taken and averaged with the scale oriented horizontally, and another 30 were taken in the vertical orientation. The horizontal and vertical average length measurements were found to differ by less than 0.1%, which was deemed acceptably similar and attributed to human measurement error. For microscope images, 1/64 in. was found to equate to 592.36 pixels. This calibration was repeated for the macro imaging setup, which equated 1/64 in. to 65.94 px. Converting units from dots per inch (DPI), the micro images have a pixel width of 0.00066999 mm/px and the macro images have a pixel width of 0.0060189 mm/px. These conversion factors are the basis for all analysis beyond a simple PAC calculation, and thus should be verified with some regularity over long test campaigns to ensure reliable data output.

Overview of Segmentation Algorithm

The following steps are used to identify and characterize individual particles within an input microscope image against the elastomer seal background. This algorithm was developed to minimize two common sources of error: misclassifying clusters of several small particles as a single large particle and mistaking surface features or texture of the elastomer as a particle. The corresponding Matlab function is provided for each algorithm step as an example of how the algorithm could be implemented.
Consider the raw input image shown in Figure 11, depicting JSC-1A simulant deposited on the crown of an NDS seal.

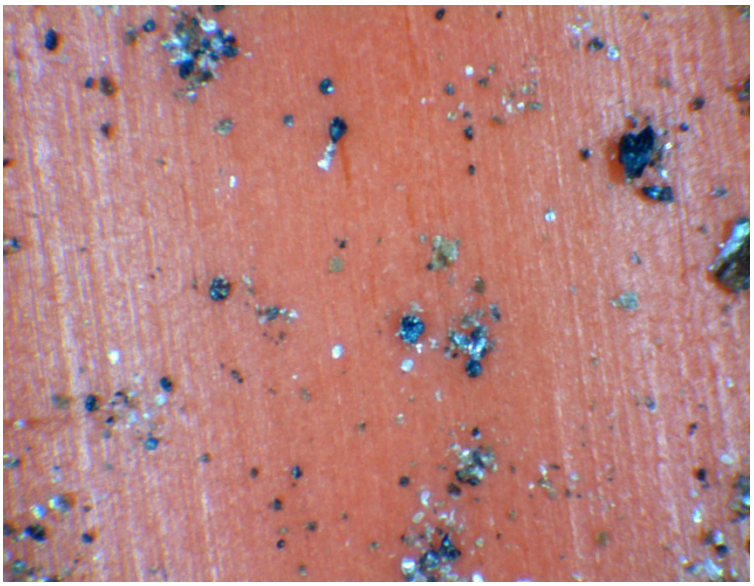

Figure 11.—Unmodified input image.

The first image transformation is a conversion from the RGB (Red/Green/Blue; cartesian) color model to HSV (Hue/Saturation/Value; cylindrical). This is achieved with the ‘rgb2hsv’ function. The ‘Hue’ channel is isolated and used for subsequent transformations, flattening the image array to two dimensions. This channel was found to have the most variation between elastomer and particle, yielding more accurate segmentation. The resulting image is shown in Figure 12.

The image shown in Figure 12 is then subjected to a contrast-limited adaptive histogram equalization (often referred to as ‘CLAHE’), which enhances the contrast of the image to exaggerate the differences between particle and elastomer. The ‘adapthisteq’ function is used to perform this transformation to produce the image shown in Figure 13.

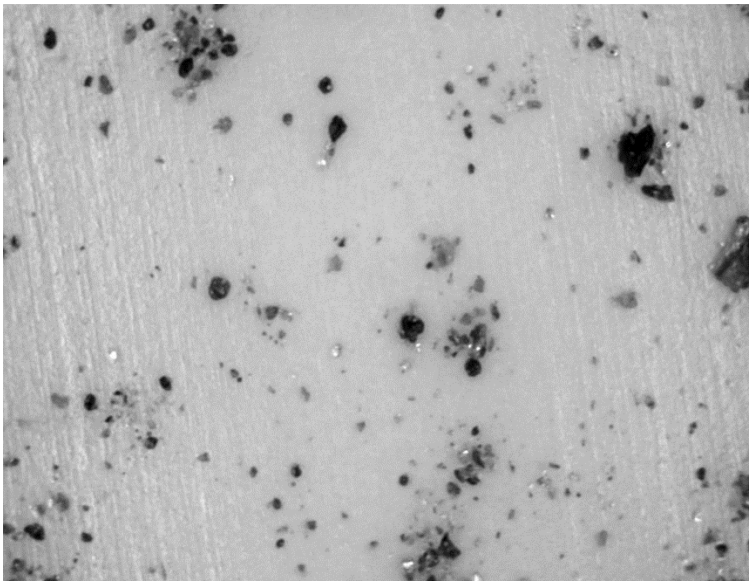

Figure 12.—Hue channel shown in grayscale.

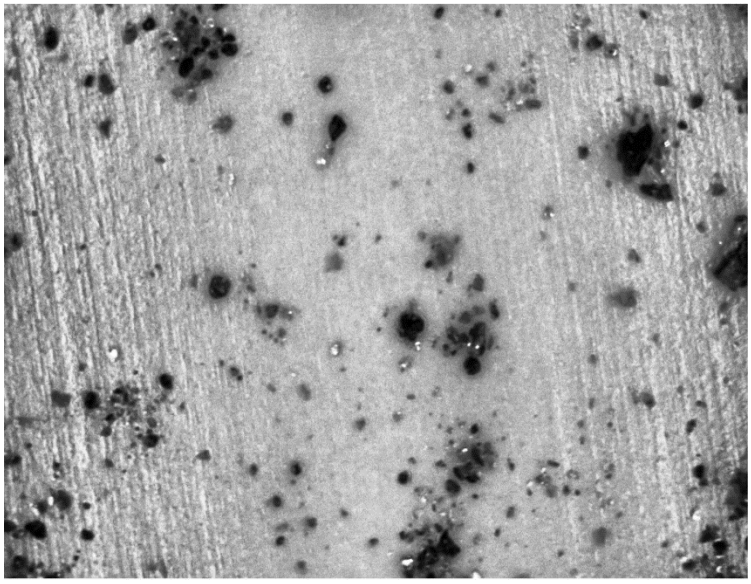

Figure 13.—Image contrast improved with CLAHE.

The ‘imbinarize’ function is then used to distinguish ‘foreground’ (particles) from ‘background’ (elastomer surface). This differentiation is on a local basis, which is key to mitigating the changes in lighting caused by any curvature in the seal surface (notice in Figure 11 that the left and right sides of the image appear generally lighter as the elastomer surface curves below the focal plane). The ‘imbinarize’ function accounts for such changes in background appearance and instead only considers the nearby background when classifying a given feature. The resulting binary image is shown in Figure 14.

A series of refinements are then made to the binary image. First, the function ‘imfill’ is used to fill in small holes and gaps. The function ‘imopen’ is then used (an erosion, followed by dilation) to fill in small concavities and smooth the boundaries between particle and elastomer. Lastly, the function ‘bwareaopen’ is used to remove clusters deemed too small to be particles. This step is particularly useful in distinguishing between elastomer surface texture and particles. It is worth noting that the resulting binary image, shown in Figure 15, is not being used directly for segmentation. Comparing Figure 14 and Figure 15 it can be seen that, counterintuitively, clusters of particles tend to get filled in and grouped together. The aim at this stage is to create a clipping mask that captures all particles while not yet differentiating between the particles themselves.

Elementwise multiplication of Figure 15 and Figure 13 results in Figure 16, which is effectively the contrast-enhanced image cropped around each particle. Removing the background in this way while preserving surface detail for each particle enables more accurate differentiation between large particles and clusters of several smaller particles.

A search for regional extrema is now performed within the cropped image using a foreground extended maxima transform (the ‘imextendedmax’ function). This effectively breaks up clusters of particles since, locally, enough detail has been preserved to differentiate between adjacent particles. Figure 17 shows the effect of this transformation. Notice in the expanded frame to the left of the image how the original cluster outline is shown, and constituent particles are represented as filled in areas. It can also be seen that single, large particles are mostly unaltered using this approach.

Figure 14.—Binarized image.

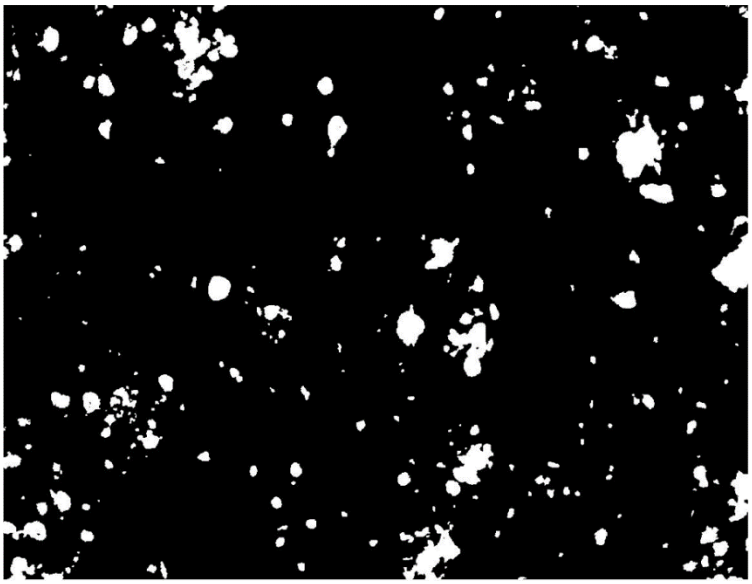

Figure 15.—Refined binary mask.

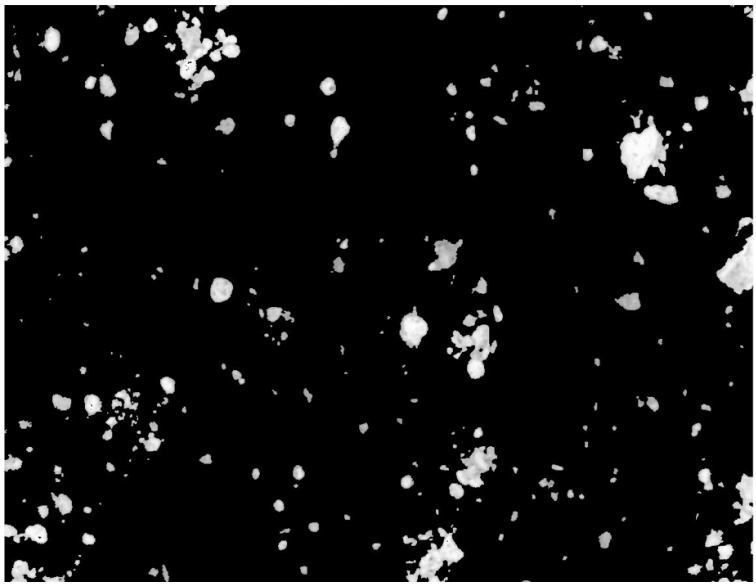

Figure 16.—Image cropped around particle locations.

This new binary mask, however, still does not contain accurate information about the boundaries of each particle. More importantly, it contains exactly one region per particle that is a subset of the true particle area. Thus, this mask can be used to ‘seed’ Figure 16 with severe local extrema such that the gradient contains one distinct peak per particle. This is accomplished by replacing a given element in the array shown in Figure 16 with the value furthest from the background value if that element is highlighted in Figure 17. The magnitude of the gradient of the resulting array is shown in Figure 18. The ‘imimposemin’ function is used to achieve this, ensuring that local extrema only occur at the peaks identified in Figure 17.

An enveloping area is created for each particle using a watershed transform, which generates boundaries that maximize the distance to nearby local maxima. The ‘watershed’ function is used in Matlab to achieve this, shown in Figure 19. These borders, formed in locations where particles are least likely to be present, are then used in the following step to define a global minimum.

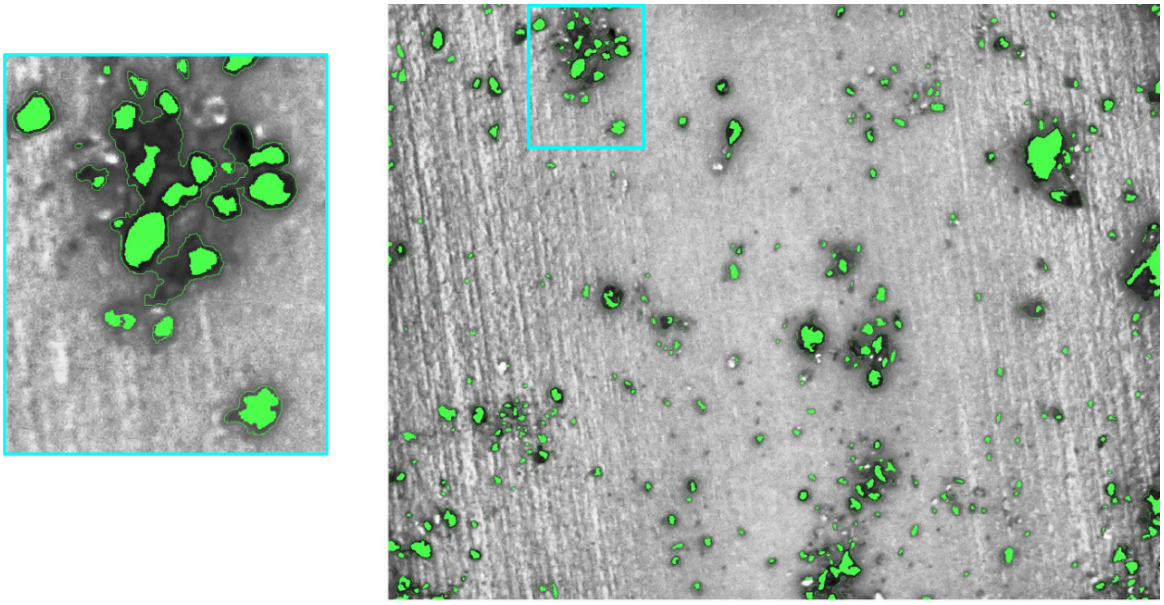

Figure 17.—Local extrema used to identify individual particles within clusters (zoomed view of cluster on left).

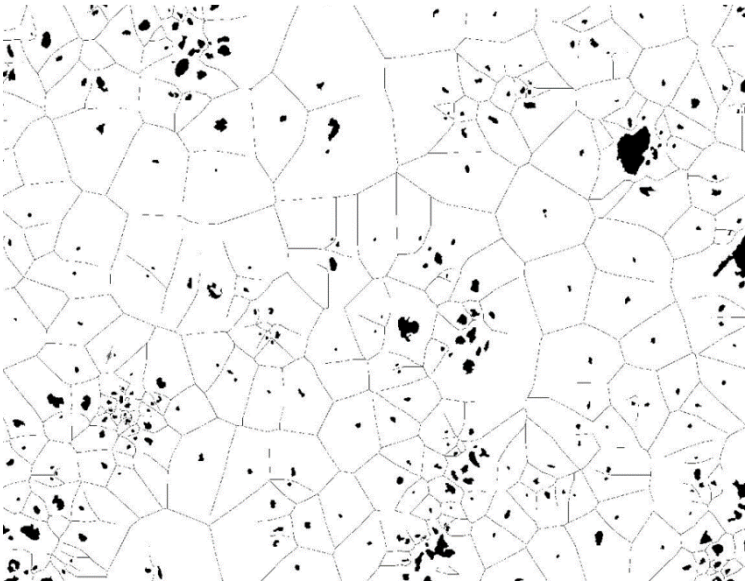

Figure 18.—Gradient magnitude with imposed regional extrema.

Lastly, a marker-controlled watershed transform is performed on the modified gradient generated using Figure 17. At this stage, the image gradient has been supplemented with two pieces of information: local maxima (peaks) that correspond to particle locations within tight clusters, and global minima (valleys) that correspond to background regions farthest from any particles. The same ‘watershed’ function is used to perform this operation which results in the segmentation shown in Figure 20.

Augmenting the gradient with additional information about particle locations enables the breaking up of tight clusters of particles. The use of a watershed transform also allows for panoptic segmentation, where each particle receives a unique identifier and can be analyzed independently of other neighboring particles. This enables subsequent analysis of particle shape, size, and location whereas something like a binary thresholding approach would only be able to measure PAC.

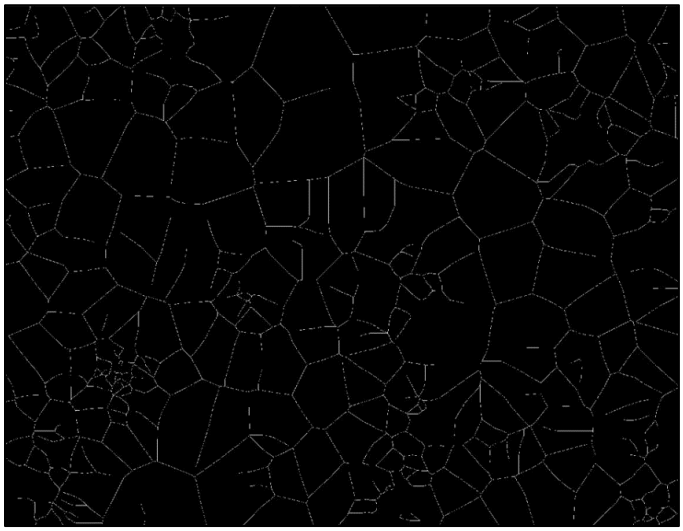

Figure 19.—Background watershed ridge lines.

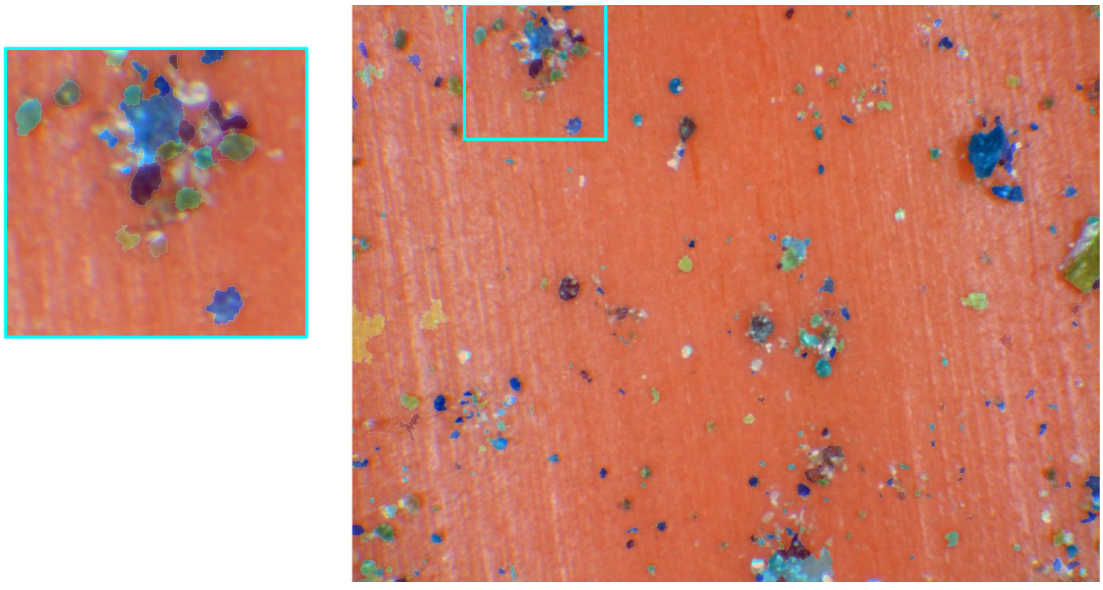

Figure 20.—Original image overlaid with segmentation results.

Post-Segmentation Analyses

Once an image is segmented, it can be used to investigate the parameters of interest discussed previously. This section outlines how those metrics are generated using the outputs of the segmentation algorithm described in the previous section.

After segmentation, each particle's size and shape are approximated with a best fit ellipse using the Matlab 'regionprops' function. The result is an object of type 'struct' with one row per particle and each row configured to include that particle's centroid coordinates, major and minor axes lengths, and major axis orientation. This step can be visualized by overlaying each ellipse onto the original image as shown in Figure 21.

This is where the process outlined in 'Calibration of Pixel Width' becomes useful. Until now, all location and size information have been measured in pixels. With a calibrated scale factor, though, ellipse parameters can be converted into a more useful length unit (i.e., millimeters). Each ellipse major and minor axis length is multiplied by this scale factor, and a new array of ellipse information is generated. Minor axis lengths are considered since this smaller dimension governs which particles would fit through a sieve of a given size during the dust deposition process.

This same particle size information shown in Figure 22 can be processed into the more common PSD form, which instead describes the proportion of particles smaller than a given size. The PSD for the original image shown in Figure 21 is shown below in Figure 23. The PSD for the JSC-1A simulant used is also shown for reference, as reported by Zeng et al.

The simulant preparation procedure outlined by Gerdts et al. (2022) was used for the dust depositions photographed and examined in this report. Consequently, the PSD presented by Zeng et al. had to be cropped to contain only particles below 0.25 mm since particles larger than this were removed via sieve during simulant preparation. The PSD estimated from the best fit ellipses shows bias in favor of smaller particles, which could be due to many factors. It is likely that the segmentation algorithm is sometimes incorrectly interpreting surface features on a single large particle as several smaller particles. It is also possible that the age and manipulation of the simulant being used has caused some degradation, gradually producing a higher concentration of smaller particles from the larger ones as they erode.

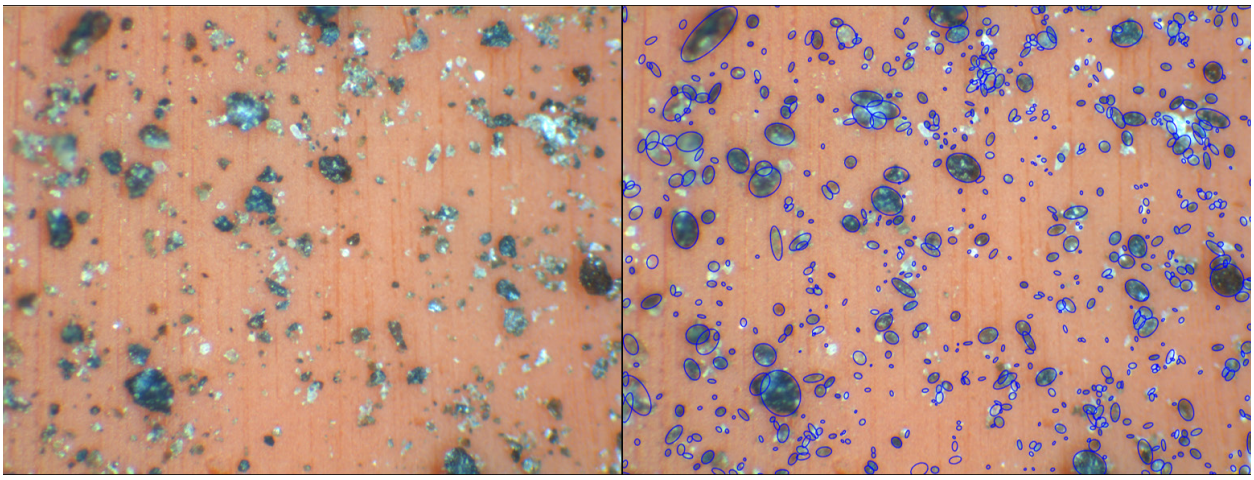

Figure 21.—Original image (left) and overlaid best fit ellipses (right).

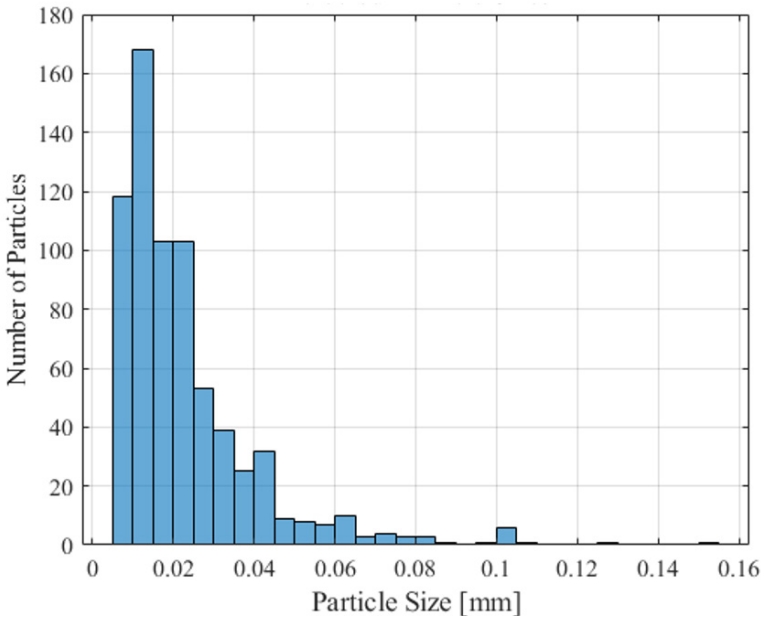

Figure 22.—Histogram of detected particle sizes.

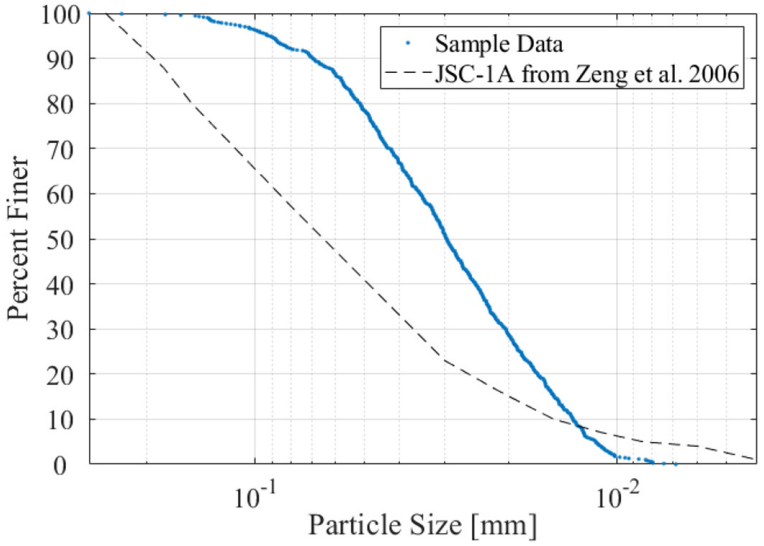

Figure 23.—Detected PSD compared to literature data.

A polar histogram can be constructed from the list of major axis orientations as a qualitative way to monitor the amount of elastomer/background surface features that are misclassified as particles during segmentation. Extrusion processes, mold textures, and the application of greases to a seal surface can all result in highly directional surface textures. Such textures can be seen clearly in Figure 24, showing a pristine NDS seal containing microscopic ridges imparted from the mold used to form the seal (left) and streaks created by wiping Braycote® Micronic 601 EF grease (BP Lubricants USA Inc.) onto a seal surface (right).

These textures, if misinterpreted as particles, manifest in the polar histogram as distinct peaks whose orientation aligns with the directionality of the image textures. Figure 25 depicts two such histograms. The left is one where filtering parameters were poorly adjusted, and as a result many north-south oriented particles were detected that were primarily artifacts of surface texture. The right plot shows a more common distribution of particle orientations that is much more uniform and does not raise any concerns about segmentation accuracy. The nature and orientation of surface textures can vary greatly depending on the material receiving the dust deposition. A visual summary of many such common surfaces with varying levels of dust depositions was presented by Jimenez in 2022 (Ref. 9) and again more comprehensively by Jimenez and Gerdts (Ref. 10).

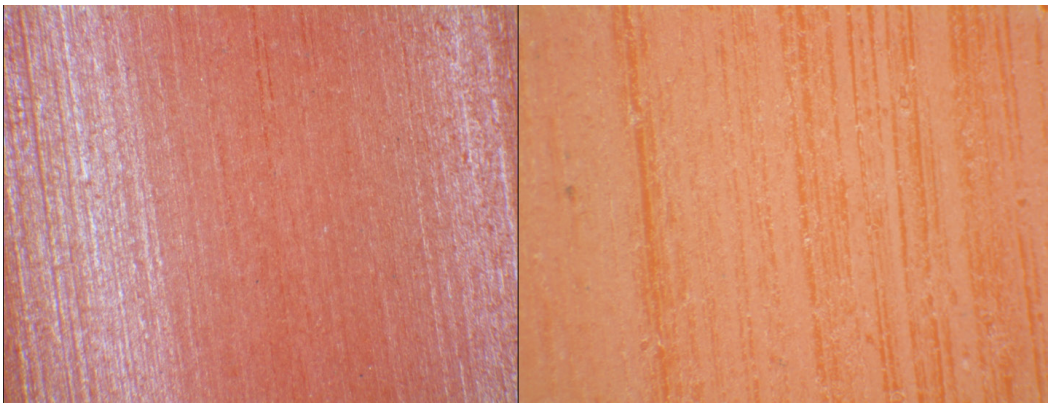

Figure 24.—Pristine NDS seal surface texture (left) and Braycote streaking on a clean seal (right).

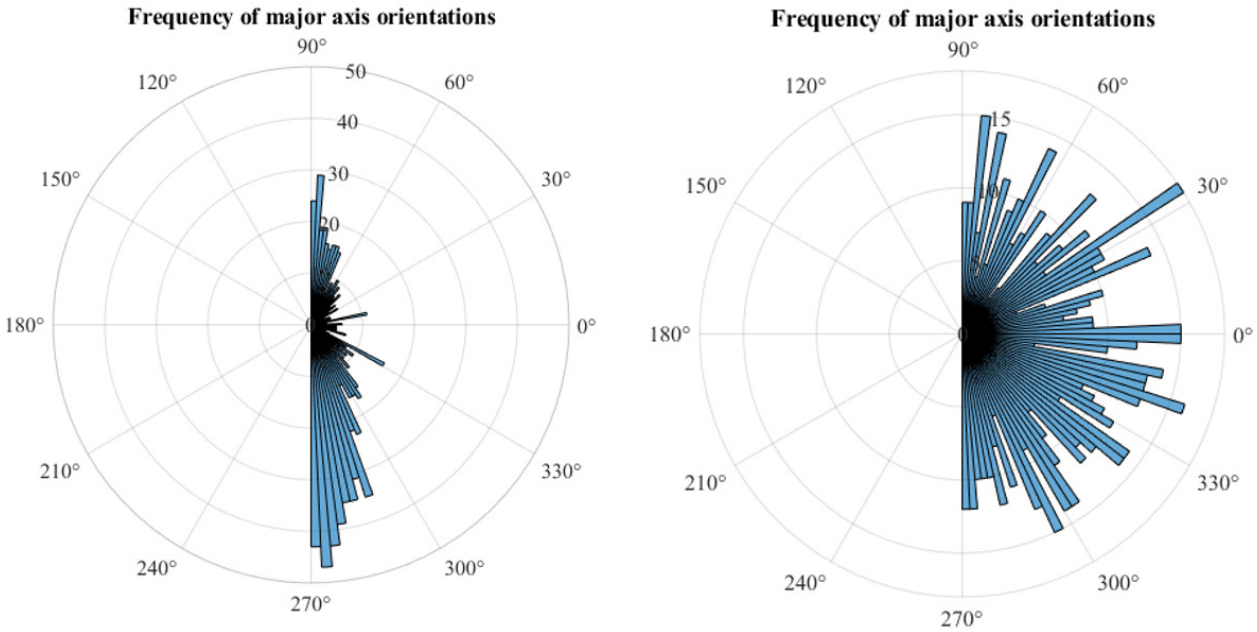

Figure 25.—Surface textures erroneously classified as particles (left) and correctly filtered (right).

One step beyond the approximation of each particle as an ellipse is the revolution of that ellipse around its major axis to form an ellipsoid. This rough approximation of a particle in three dimensions allows for the estimation of the dust mass surface density. Historically, dust contamination characterization and testing has employed either a PAC-based approach or a dust mass surface density approach. As explained in more detail in the 'Correlating PAC with Dust Mass Surface Density' section, it is often difficult to measure both parameters directly while still producing a valid test article. The generation of particle ellipsoid approximations enables dust mass surface density calculations to be made from microscopy images using available mineral densities and simulant mineralogical compositions.

To start this process, an ellipsoid is generated for each particle, along with the corresponding volume. The volume for all ellipsoids is summed for all detected particles. This volume is multiplied by an 'effective' material density for the simulant being used—that is, a weighted average of each constituent mineral density where weights are given by the proportion of the simulant a given mineral comprises. This step is required because the segmentation algorithm cannot differentiate between different mineral types, instead broadly classifying all particles together. Perhaps more sophisticated segmentation approaches could increase accuracy by recognizing particles belonging to various mineral types and calculating their masses directly.

Once the total particle volume is multiplied by the effective material density, this mass value can be divided by the total elastomer surface area captured in the image (calculated using the same pixel-to-length scale factor as described previously to convert image dimensions from pixels to mm). The ability to approximate dust mass surface density from image data allows for measurements to be taken directly on the test article rather than indirectly from a separate deposition or test surrogate. The in-situ characterization of the deposition without altering the dust in any way enables quicker, more accurate measurements to be taken while still allowing the test article to be used in other testing.

Deposition System Program for In-Situ Deposition Measurement

All the functionality described in the 'Overview of Segmentation Algorithm' and 'Post-Segmentation Analyses' sections has been compiled into a standalone executable file that can be installed on the computer used to control dust depositions and take microscopy images. With a setup such as the UDDS, this enables the monitoring of a dust deposition in near real-time without having to remove the test article from the glove box. The operator simply needs to deposit the dust, capture a microscope image, and analyze it using the application (or analyze multiple images from various locations for additional confidence in the true level and uniformity of the deposition). If targeting a specific deposition level (e.g., 18% coverage), this iterative process can be repeated as the amount of deposited dust gradually accumulates to the desired level. If too much dust is deposited and the measured PAC exceeds the target value, the test article must be removed from the UDDS and cleaned before the buildup of deposited dust is restarted. The time-consuming nature of this reset makes the fine control of the UDDS over single-pass deposition level (characterized by Gerdts et al. in 2022) extremely useful in targeting specific PAC levels without overshooting (Ref. 11). The current version of the UDDS at GRC can reliably deposit dust to within ±0.5% of the desired PAC. The image analysis program takes around 15 seconds to process an image, and the intensity of a single deposition pass can be varied from less than 1 PAC increments per cycle all the way up to around 50 PAC. The user interface for the program is shown below in Figure 26.

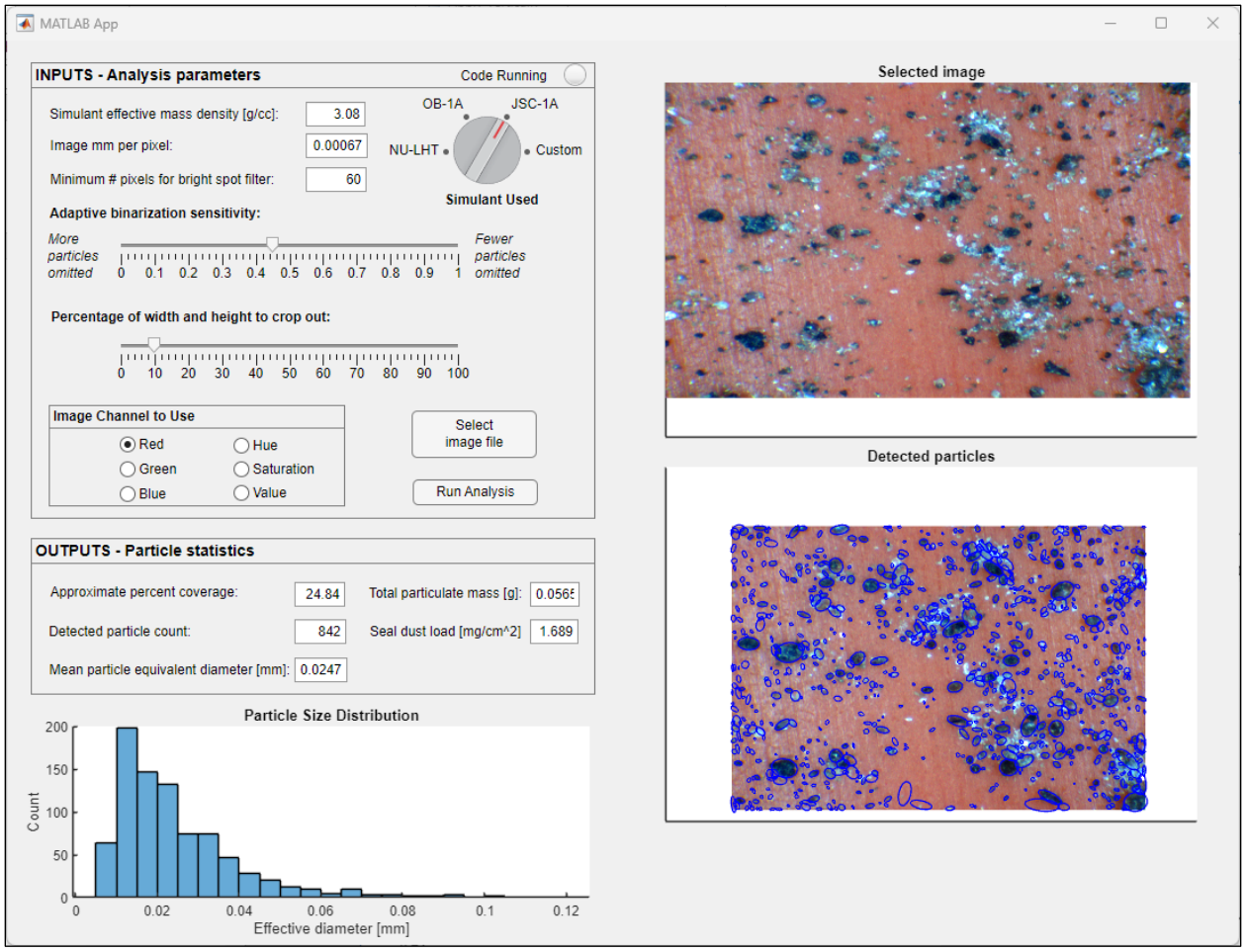

Figure 26.—UDDS Deposition monitoring program user interface.

The program is preloaded with convenient information like the ‘effective material density’ as described previously for various simulants, which can be selected using the graphic user interface (GUI) knob. Image processing parameters are similarly adjustable but initialize to preset values to allow consistent ‘default’ analysis settings to be used for most applications. The program allows users to select an image file from a local directory, and it outputs key metrics like PAC and estimated dust mass surface density alongside a visual aid depicting all detected particle best fit ellipses. The measured PSD is also shown in the GUI window.

Batch Processing Script for Full Deposition Characterization

The program developed for the UDDS was intended for quick in-situ measurements of surface coverage during the deposition process. Once a deposition is complete, however, additional microscope images must be collected to ensure confidence in the level and spatial uniformity of the deposition. Several images are taken uniformly spaced around the surface that received the dust deposition and are all stored in a unique folder per deposition. A Matlab script was written to repeat the analysis summarized in the ‘Overview of Segmentation Algorithm’ section over all images contained in a user-input folder, allowing an entire deposition to be characterized at once. This script outputs a summary containing the PAC and estimated dust mass surface density for each image analyzed. The script then calculates a

sample mean and standard deviation to statistically describe the dust deposition as outlined in the 'Sampling Statistics Considerations' section.

Exploratory Ideas

Correlating PAC With Dust Mass Surface Density

The direct measurement of σ_{dust} usually necessitates the disturbance of the test article with the use of masking or witness samples as described in NASA-STD-1008 Section 5.2.1.1.d (Ref. 12). Image-based PAC analysis does not have this impact and is much more easily implemented in a nondestructive manner to characterize in-situ dust deposition levels directly on the surface of a test article. However, PAC is not always a convenient unit of measure for system-level requirements. If an adjacent system or activity is expected to generate a known mass of dust, for example, then it would be logical for nearby systems to write requirements in g/cm^2 rather than PAC, since this value could more accurately be estimated based on available information.

The empirical conversion from PAC to σ_{dust} has been considered and attempted with varied results as reported by Hurlbert et al. in 2023 and Quick et al. in 2024 (Refs. 6 and 13). This report expands upon this effort, presenting additional test data connecting PAC measurements directly with mass measurements per NASA-STD-1008. This body of work also highlights some simulant-specific considerations that must be made when attempting to approximate σ_{dust} from PAC measurements.

To allow PAC and σ_{dust} measurements to be taken directly from the same deposition, the test fixture shown in Figure 27 was constructed. The fixture allows half (circumferentially) of a seal surface to receive a dust deposition as normal, with the other half containing witness sample assemblies. These witness sample assemblies consist of a sample holder and sample mask. The sample holder is an acrylic frame with an annular window cut through the middle that matches the inner and outer diameters of the test seal and spans a 15° arc. A piece of Kapton® polyimide tape is placed over this window with the adhesive facing upward. Each sample holder is positioned below a mating sample mask with two alignment pins. The sample mask's purpose is to prevent dust from being deposited anywhere on the sample holder except for the polyimide tape, whose adhesive helps limit dust migration from the surface once deposited.

The mass of each of the six test sample holders was measured three times to the nearest 0.01 mg using an Ohaus EX225/AD electronic balance (with a measurement accuracy of ±0.0001 g) with the average value recorded. This process was repeated for an additional six identical sample holders, which would serve as a control group. The test sample holders were loaded into the test fixture, which was then positioned over the test seal. This assembly was loaded into the UDDS along with the six control group sample holders. A deposition was performed on the test assembly, while the control group was kept far away and shielded from any sources of dust while inside the UDDS glovebox. Microscope images of the exposed half of the elastomer seal were taken following the same procedures as a typical deposition before unloading the test and control samples from the UDDS. The sample masks were removed from each sample holder, being careful not to disturb the dust that had accumulated on either part. The mass of each sample holder was then recorded three times with the average taken. The mass of each of the control group sample holders was also recorded three times and averaged (all test and control group sample holders received a unique identification number so the mass for each could be compared before and after deposition).

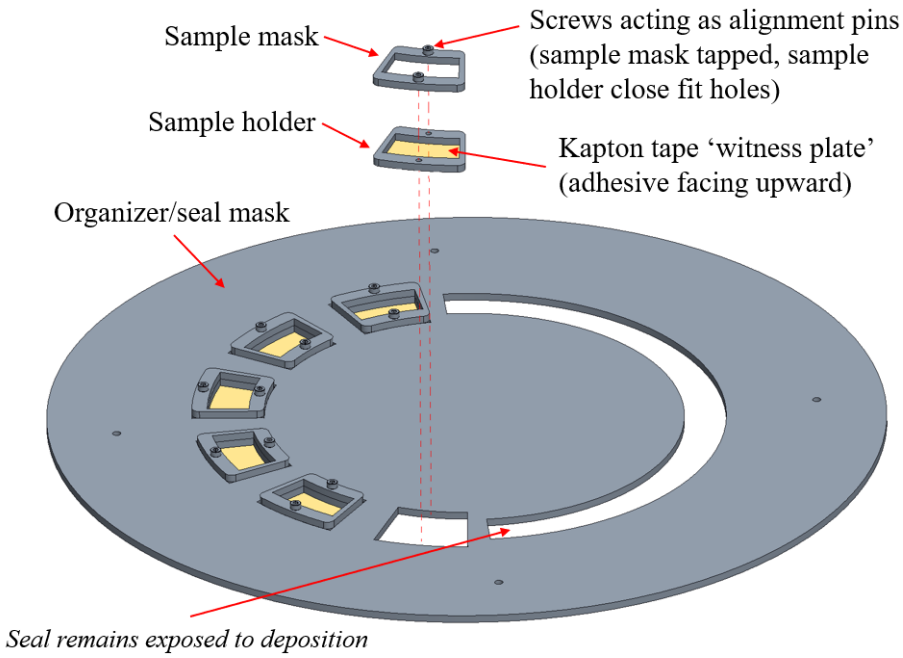

Figure 27.—Witness sample fixture assembly.

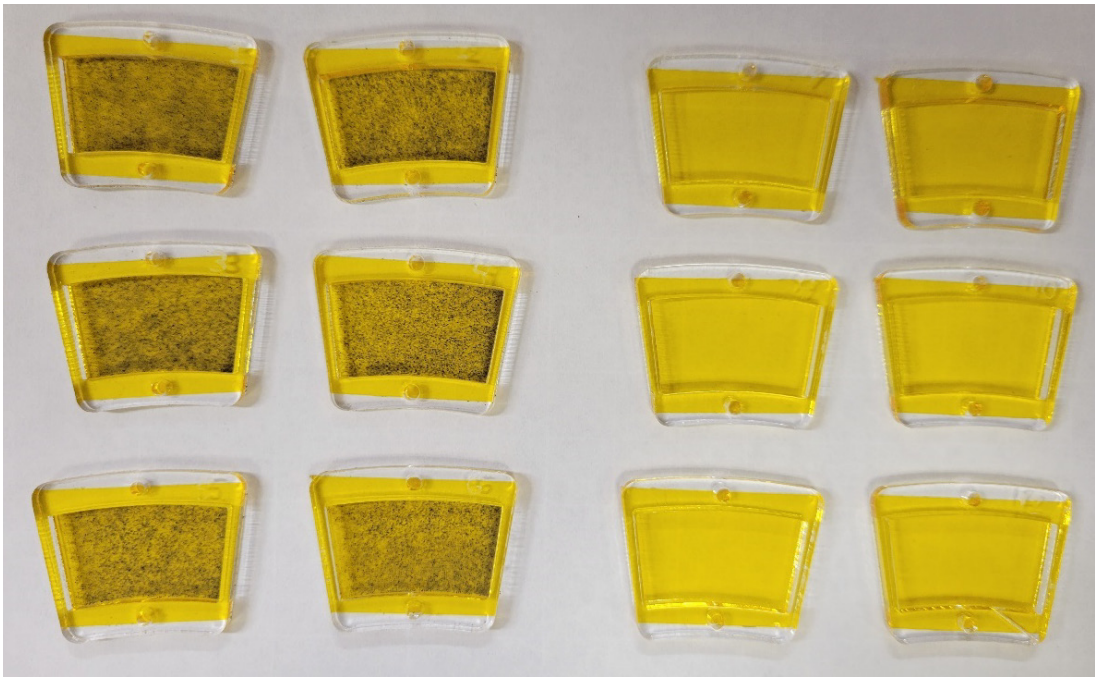

Figure 28.—Sample holders from the test (left) and control (right) groups.

The microscope images of the seal were used to calculate the deposition PAC, while the change in mass measurements pre- and post-deposition were used in conjunction with the surface area of the exposed polyimide tape to calculate the dust mass surface density. Three depositions were performed using this methodology. All surfaces were thoroughly cleaned with isopropyl alcohol, and the polyimide tape was replaced for all sample holders between depositions. Using the effective material density value discussed for JSC-1A simulant, a blind prediction of σ_{dust} was calculated for each deposition based on the

image segmentation approach described in the ‘Post-Segmentation Analyses’ section. The resulting comparison between PAC and σ_{dust} is shown in Figure 29.

An alternative visualization for the data presented in Figure 29 is to group the data points by deposition. Figure 30 does this, demonstrating reasonable alignment between the two approaches.

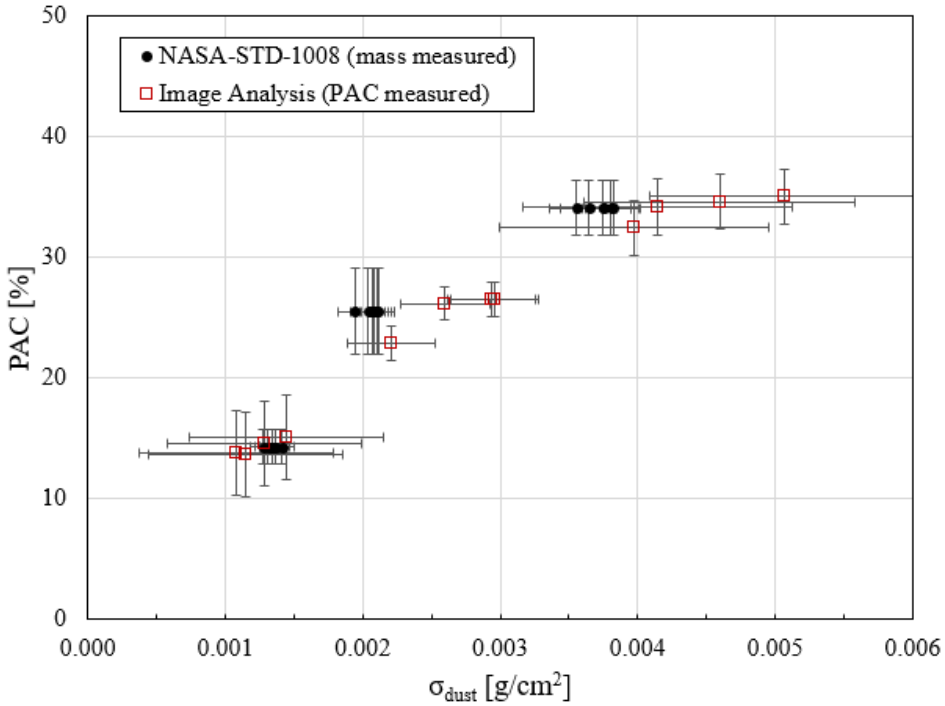

Figure 29.—Direct measurements of PAC and σ_{dust} compared for JSC-1A simulant

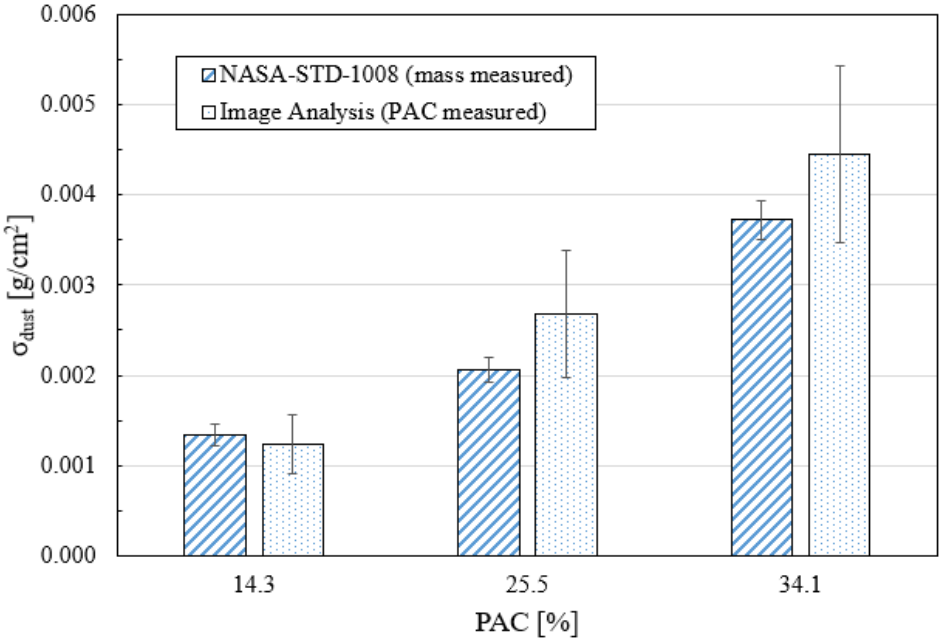

Figure 30.—σ_{dust} estimates using direct mass measurement versus image analysis.

The accuracy of σ_{dust} estimations from PAC measurements hinges upon accurate knowledge of the deposited particle size distribution. Consider two depositions with an identical PAC: one achieved using a coarse simulant containing almost exclusively large particles and another of only very fine particles. Now consider total particulate mass for each deposition. Despite identical PAC measures, the deposition using the finer particles will have a lower mass. This is because, in the limit as particle size approaches zero, the volume occupied by the particles deposited on the surface approaches a very thin film. Contrast this to the larger particles, which occupy significantly larger volumes normal to the image plane to achieve the same effective PAC.

To demonstrate this, the simulated deposition script discussed in the 'Methods for Quantifying Segmentation Error' section was used. Because this script simulates dust depositions with a user-defined PSD, parameterizing this value was straightforward. Figure 31 shows the results of increasing and decreasing the PSD of JSC-1A simulant by various scaling factors, all achieving the same PAC.

Simulated depositions were completed with a total of five different input PSDs, all scaled up or down from JSC-1A's PSD. For each simulant variation, ten depositions were simulated for PACs ranging from 5% up to 50%. The resulting images were fed into the UDDS deposition characterization script outlined in the 'Current Image Processing Methods' section, with PAC and σ_{dust} values recorded. A summary of the results is shown in Figure 32, confirming the impact of PSD on the ability to correlate PAC to dust mass surface density.

This clear trend highlights that, however inconvenient, there cannot exist one single conversion factor used to convert PAC to σ_{dust}. Instead, this conversion must be simulant-specific and account for differences in PSD. This PSD dependency could partially explain the differences between the data generated above with JSC-1A simulant and the trends presented by Quick et al. using both LHS-1D and NU-LHT-4M simulants (Ref. 13). The above analysis could be repeated using the PSD of each simulant for a more direct comparison. Additionally, this would provide insight to the impact of the shape of the PSD rather than purely its scaled magnitude as demonstrated in Figure 32.

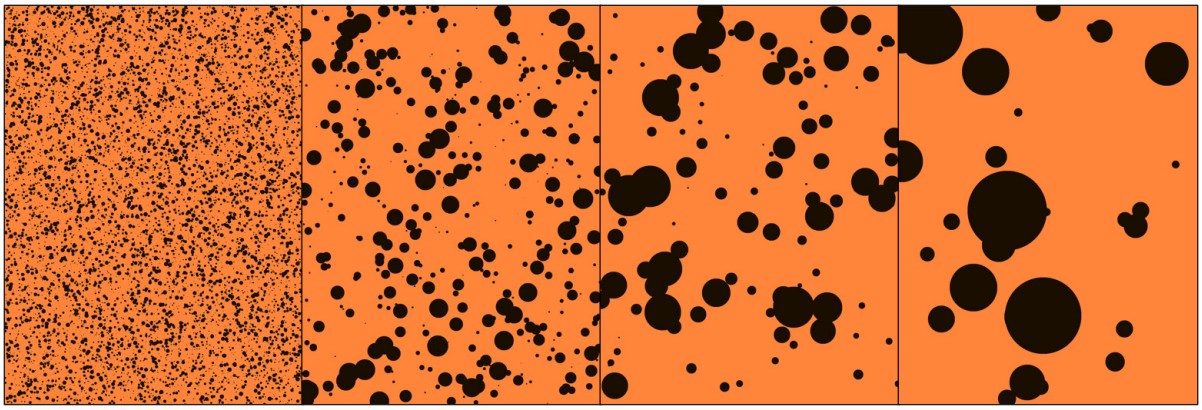

Figure 31.—Simulated 20 PAC depositions of JSC-1A simulant with altered PSDs.

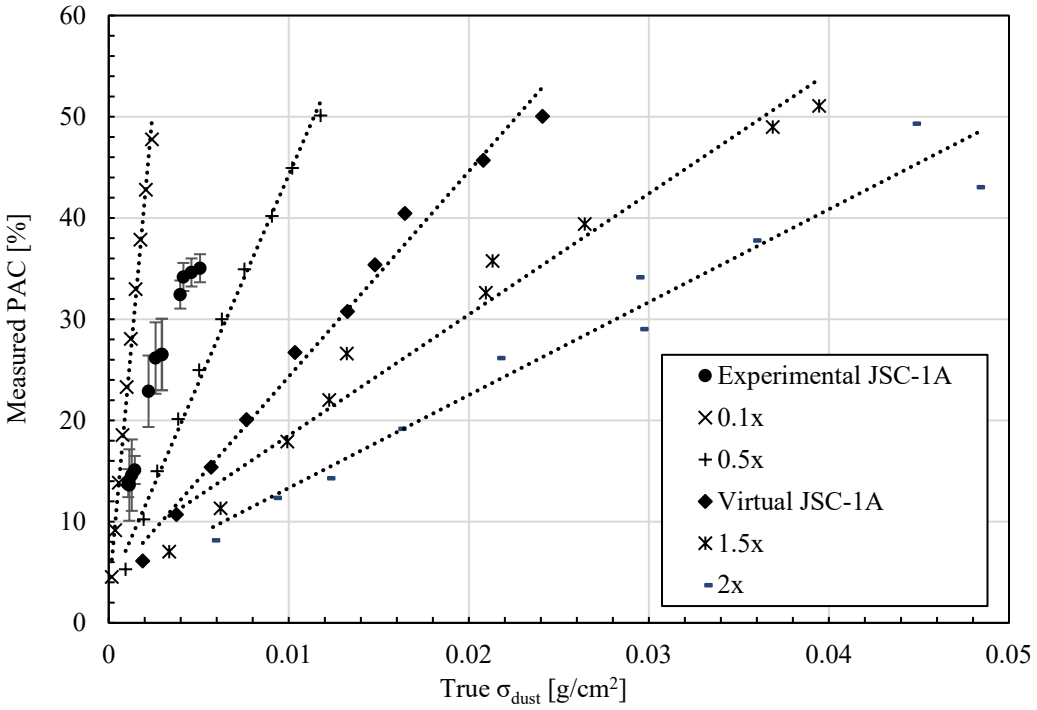

Figure 32.—Impact of PSD on PAC-σ_{dust} correlations.

Note the location of the 'Experimental JSC-1A' data in Figure 32, residing between simulated depositions with particles 10% and 50% the size of JSC-1A simulant (this experimental data is from the NASA-STD-1008 direct mass measurement methodology presented in Figure 29). There are a couple of factors that likely contribute to the discrepancy between virtual and experimental JSC-1A trends, which indicate that the simulant used experimentally had smaller particles than a nominal JSC-1A simulant. The simulant preparation process outlined in NASA-STD-1008 and NASA/TM-20210024128, used for all dust depositions in the UDDS, involves rolling the simulant in a sealed cylindrical container on a lab roller for 30 minutes. This rolling process likely reduces some portion of the larger particles and shifts the overall PSD finer. Additionally, it is likely that the segmentation algorithm is not completely effective at avoiding the classification of large particles as multiple small particles (a couple minor instances can be observed in the ellipses shown in Figure 21). The measured PSD of deposited JSC-1A simulant shown in Figure 23 confirms that a PSD biased towards fine particles was used for σ_{dust} approximations and supports the trend shown in Figure 32 that suggests the experimental JSC-1A simulant was actually finer than the JSC-1A PSD available in the literature. Such agreement indicates the utility of the simulated deposition script for estimating PAC-σ_{dust} conversions in a way that accounts for PSD.

A recent area of study for non-destructive in-situ dust measurement is the use of portable x-ray fluorescence spectroscopy (pXRF) devices (Ref. 14).While the methods described by Liftosky et al. only yield σ_{dust} measurements (no microscopy imaging was reportedly used, and thus no PAC measures), this new pXRF technique could be coupled with the imaging analysis presented in this body of work to further validate both methods. Agreement between the pXRF σ_{dust} measure and the estimated σ_{dust} derived from image analysis would indicate that either method can be reliably used depending on availability of equipment, convenience, and precision required.

Leak Path Length Measurement—Pathfinding Approach

The goal of most surface dust contamination characterization is to establish a correlation between contamination level and some other application-specific performance parameter. Dust-tolerant seals development, for example, aims to monitor the impact of dust deposition level on seal leak rate. Conventionally, PAC has been used as a measure of surface contamination level because it is relatively easy to measure without disturbing the unit under test. Alternatively, dust mass surface density has also been used because of its convenient units from a systems engineering perspective, where a surface's exposure to a known quantity of dust can be predicted. These two approaches are not exhaustive; there are other measured and calculated parameters that can be compared with seal leak rate that may reveal useful correlations.

One such proposed parameter is the 'effective leak path length' across a sealing surface: the shortest possible path across the seal, where the space occupied by particles is considered without penalty. The intent behind this definition is to capture the relative ease gas molecules have passing through the tented void created around particles where the elastomer seal cannot perfectly conform around the particle and therefore loses contact with the opposing sealing surface locally. This section outlines one approach to calculating this parameter using micro images.

To explore this idea, an A* pathfinding algorithm was set up to iteratively find the 250 shortest paths from the leftmost column of pixels to the rightmost (the direction of leaking air flow across test seals). A segmented binary image was used, where background pixels had value 1 and particles had value 0. The cost scheme was setup such that a pixel's value represented the cost incurred by travelling though it: gas molecules were 'free' to pass through/around a particle, while they were penalized for travelling across the seal surface. The results are visualized in Figure 33, with the shortest leak paths appearing the brightest.

Because of the large image dimensions, this pathfinding approach is computationally expensive. Especially if several shortest path lengths are desired, the A* algorithm quickly becomes time-prohibitive in this application. For this reason, analyzing enough images to establish a correlation between shortest effective path length and leak rate was not attempted.

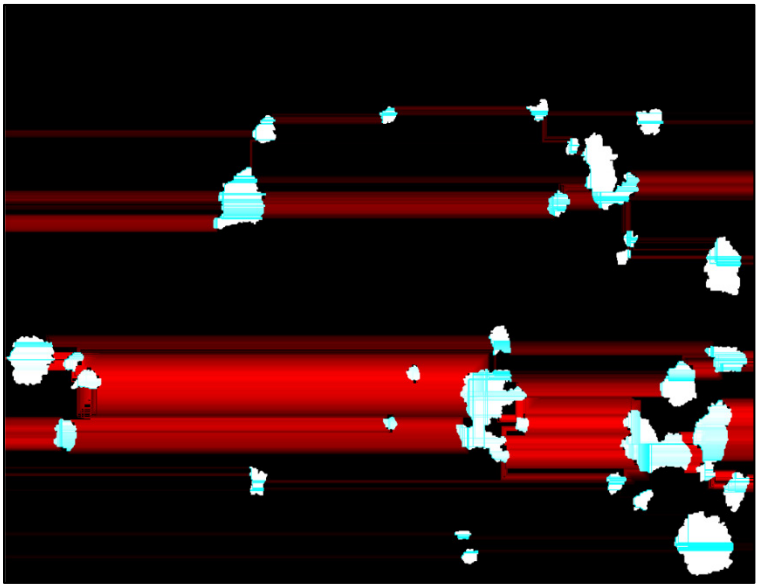

Figure 33.—A* pathfinding applied to dusty seal surface.

Leak Path Length Measurement—Network Approach

The use of weighted networks presents an alternative approach to determining the shortest leak path across an image of a dusty seal. An undirected network *G* was constructed according to Equation (5).

$$G = (V, E) \tag{5}$$

where *V* is the set of all vertices and *E* is the corresponding set of edges. Both *V* and *E* are weighted sets. After image segmentation, each particle's best fit ellipse was used to calculate an 'equivalent radius,' denoted r_{eq} and defined as the radius of a circle whose area is the same as that of a given particle's silhouette. It is assumed that the inherent symmetry of the orientation of particle major axes being uniformly distributed negated potential error introduced by using r_{eq} rather than ellipse radii oriented on a case-specific basis. Vertex weights for the i^{th} particle were defined per Equation (6).

$$V_i = r_{eq,i} \tag{6}$$

To construct the edges of the network, an n-nearest-neighbor search was performed on all nodes, with n=50. This resulted in 50 node pairs for each element in *V*, which collectively comprise the set *E*. This edge set *E* was used to construct an adjacency matrix *A*. For each vertex pair $\{v_j, v_k\}$, the weights for elements A_{jk} and A_{kj} were assigned by calculating the Euclidean distance between centers of neighboring vertices j and *k*. Formally, this is given by:

$$A_{jk} = \begin{cases} \sqrt{(x_k - x_j)^2 + (y_k - y_j)^2} & if\ (j,k) \in E \\ 0 & otherwise \end{cases} \tag{7}$$

where x_j and y_j are the horizontal and vertical coordinates of the particle corresponding to the j^{th} vertex in *V*, and similarly for x_k and y_k corresponding to the k^{th} vertex.

Finally, the cost of travelling from one node to another was defined as both node weights subtracted from the edge weight:

$$\mathcal{L}_{jk} = A_{jk} - V_j - V_k \tag{8}$$

This cost function definition preserves the intent to only penalize traversing across the seal surface, while traversing through or around the tented region surrounding a particle comes without cost. However, the computation time is significantly reduced because of the smaller domain (one vertex per particle, rather than one per pixel in the prior section).

A list of 'start' nodes was created by identifying all nodes within a certain distance of the left side of the image. Similarly, a list of 'end' nodes was created using the same distance threshold and the right side of the image. Dijkstra's algorithm (a commonly used 'best-first search' algorithm that guarantees the shortest path between two nodes in a graph with non-negative edge weights) was then repeated for each unique combination of start and end nodes using the cost function $\mathcal{L}$ from Equation (8), and the shortest path length for each unique combination was recorded (Ref. 15).

Figure 34 shows an example of a network overlaid onto an example micro image, where edges are visible as blue lines that connect a given particle to its nearest n neighbors.

Figure 35 shows the results of running Dijkstra's algorithm between multiple start and end nodes. The shortest paths for each combination of start and end nodes are shown as bold red lines. Vertices are

visualized with their best fit ellipses, shown in blue. Note that n=10 was used to generate Figure 34 and Figure 35 rather than the n=50 used in analysis to avoid cluttering the visualization.

The total cost of each shortest path was calculated, representing the shortest effective leak path for a theoretical gas molecule across the image from left to right. Another interpretation of the cost is the effective seal width, expressed as a percentage of the image width. Because the resistance to flow imposed by traversing through the free space around a particle is considered negligible compared to traversing across the seal surface, the cost function $\mathcal{L}$ from Equation (8) effectively accumulates a length of seal material unimpacted by particles across which a gas molecule must traverse to escape through the seal.

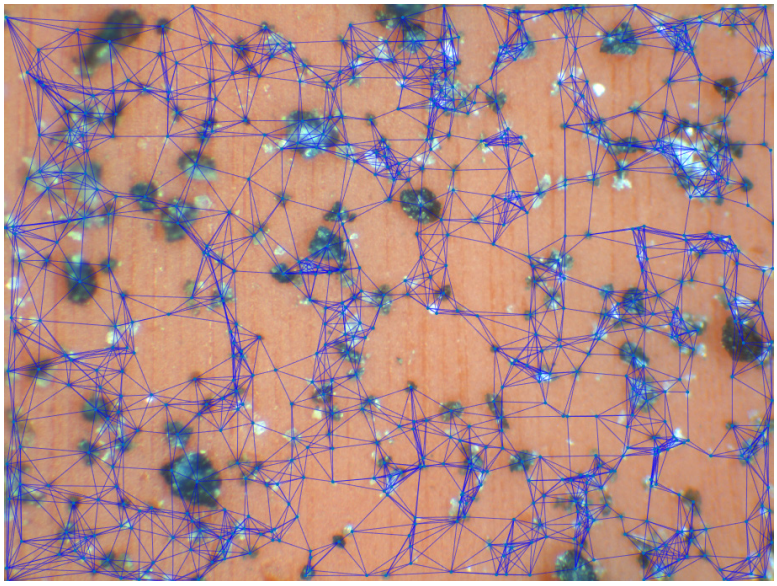

Figure 34.—Network graph overlaid onto dust deposition.

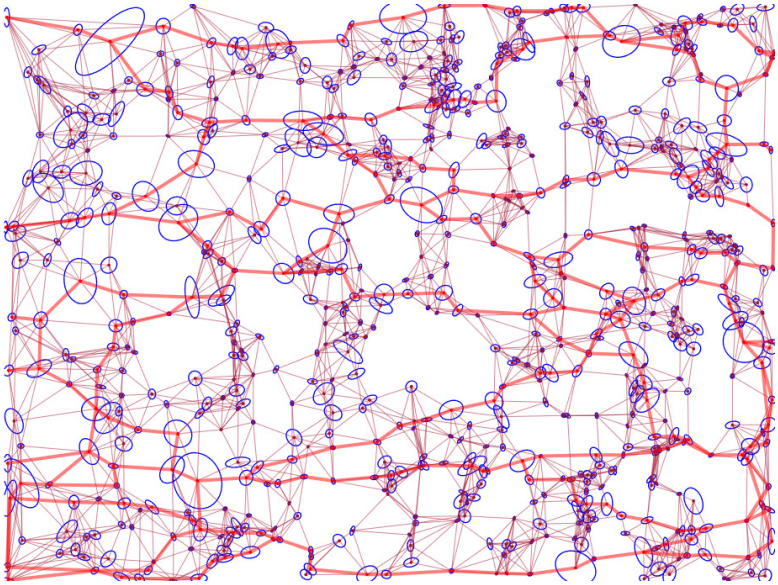

Figure 35.—Shortest paths across seal highlighted.

It is worth commenting that PAC is a very similar measure, only extending in two dimensions rather than strictly across a seal. For example, a PAC value of 25% would imply that only 75% of pixels in a randomly selected row of pixels across the image should be expected to contain seal material. Thus, the measured PAC would predict an effective seal width of 75% in this instance. The key difference between this estimate and the network-based pathfinding approach is that the network approach tests all paths, beyond the inherently random straight-line samplings of the PAC approach. Using the same hypothetical 25 PAC, it is possible that the network analysis identifies a leak path short enough to generate an effective seal width of 65%, much lower than the 75% described by the PAC. The PAC provides an upper bound to the shortest possible effective seal width, whereas the network approach finds the shortest possible value. Whether this distinction is practically significant has yet to be empirically proven. Similarly, insufficient data exists to-date to assess the reliability of shortest leak path or effective seal width as an indicator of seal leak rate. This potential utility of the network approach is one of many that merits its preliminary overview in this body of work.

Conclusions

After a brief overview of the UDDS and its specifications, the implications of image resolution on the ability to accurately detect particles and measure deposition levels was discussed. Examples were provided highlighting that specific consideration must be made to pixel width as it relates to the size of particles present on the surface. The development of the methods used for dust deposition characterization were explored.

Percent area coverage (PAC) and dust mass surface density (σ_{dust}) were identified as two primary measures of dust deposition level, each with context-specific advantages and drawbacks. Most significantly, it is easier to measure PAC without disturbing the deposition on test hardware, whereas measuring σ_{dust} directly often involves the use of masks and witness samples that prevent uniform depositions across the entire test specimen.

Three image segmentation techniques were discussed as they apply to the accurate differentiating between particle and background surface. Semantic segmentation can be less involved but is limited to PAC calculations because of its inability to distinguish individual particles. Instance segmentation is useful for determining particle count but cannot provide PAC information because of its lack of pixel classification. Panoptic segmentation provides the benefits of both methods at the cost of being more difficult to accurately implement. The uses of both conventional image processing and more modern machine learning techniques were outlined, with examples of convenient use cases for each.

The use of eight micro images to measure the PAC on a test article was justified statistically by examining the impact of reduced sample size on PAC measurement uncertainty. It was concluded that additional images per deposition had diminishing returns on PAC uncertainty, whose error was driven largely by image segmentation rather than sample size. Macro image analysis via thresholding was found to exhibit higher PAC uncertainty than micro image analysis despite having 4.5x the sample size. This increase in error can be attributed to the order-of-magnitude decrease in pixel width characteristic for the macro image setup compared to the micro images collected in the UDDS.

A new program was created to simulate dust depositions on an elastomer surface to quantify the uncertainty introduced during image segmentation. The simulation of the process results in precisely known ‘true’ PAC values, which were compared to measured PAC values after feeding the simulated deposition images through the segmentation algorithm currently employed by the UDDS. It was found that images with a pixel width below 1/1000 mm resulted in a relative error of less than 2% regardless of deposition level, whereas images with a pixel width of 1/100 mm were found to result in PAC

measurements with up to 12% relative error. This result reinforces the recommendation to use high magnification and sampling statistics to bolster measurement confidence rather than wide field of view macro images, even if they capture a larger portion of the surface in a single image.

An overview of the panoptic segmentation algorithm developed for the UDDS was provided. This algorithm augments the image gradient with additional useful information about local extrema to more effectively classify clusters of particles as such, rather than mistaking them as single large particles. It also includes diagnostic functionality like a polar histogram plot of particle orientations to ensure that highly directional surface features of the background are not mistakenly classified as particles. Using panoptic segmentation also means that each individual particle is assigned an index and can be used to estimate total particulate mass and collective particle size distribution. A graphic user interface (GUI) was developed for this algorithm and packaged into an executable file for deployment on the UDDS control computer, allowing for near real-time PAC and σ_{dust} measurements during a deposition for achieving precise deposition level targets within 1% PAC.

A series of tests were conducted to evaluate the accuracy of estimating σ_{dust} blindly from an image. Witness samples were used per NASA-STD-1008 to directly measure the mass of deposited simulant while UDDS image processing techniques were used on the remaining seal surface. The resulting image-based σ_{dust} estimates were found to successfully approximate measured σ_{dust} levels, although additional testing is required to validate and refine this technique beyond a proof of concept. It was theorized that this conversion between PAC and σ_{dust} is simulant specific, relying on the PSD of the simulant used. This trend was verified in simulated depositions where the PSD of the simulant used was scaled up or down to establish reference curves.

'Effective seal width' was explored as an alternative predictor of seal performance at a given deposition level. While insufficient test data exists to establish a correlation between this parameter (defined as the shortest possible path across a seal, excluding any particles encountered), two potential analyses were presented to generate this parameter: one using the image itself as the domain for the A* pathfinding algorithm, and another instead overlaying a weighted network with particles as vertices and a custom cost function using Dijkstra's algorithm. Both methods were successfully used to identify paths across the seal surface significantly shorter than the width of the image, with the network-based approach taking significantly less compute time.

References

1. Gerdts, Stephen; Jimenez, Nathan; and Dunlap, Patrick H. Jr.: Lunar Simulant Deposition Technique for Dust Tolerance Studies. NASA/TM-20210024128, 2022. https://ntrs.nasa.gov
2. Abdulateef, Salwa Khalid; and Mohanad Dawood Salman: A Comprehensive Review of Image Segmentation. Iraqi Journal for Electrical and Electronic Engineering, 2021, pp.166-175.
3. Al-Kofahi, Y.; Lassoued, W.; Lee, W.; and B. Roysam: Improved Automatic Detection and Segmentation of Cell Nuclei in Histopathology Images. IEEE Transactions on Biomedical Engineering, vol. 57, no. 4, 2012, pp. 841-852.
4. Rettenberger, Luca; Szymanski, Nathan J.; Zeng, Yan; Schuetzke, Jan; Wang, Schilong; Ceder, Gerbrand; and Reischl, Markus: Uncertainty-aware particle segmentation for electron microscopy at varied length scales. NPJ Computational Materials, vol. 10 no. 124, 2024, pp. 1-7.
5. Jimenez, Nathan; Gerdts, Stephen; Dunlap, Patrick H. Jr.; and Mather, Janice: Lunar Dust Tolerance Testing of Representative Seals for Lunar Surface Asset Seals. Lunar and Planetary Science Conference, Lunar and Planetary Science Institute, 2022.

6. Hurlbert, Kathryn Miller; Hollingsworth, Keith; Kurwitz, Cable; Rios, Jaime; Kanoongo, Siddarth; and Khater, Ali Zein: Design and Testing of a Device for Moon Dust Deposition on Test Articles/Systems. Thermal & Fluids Analysis Workshop, NASA Glenn Research Center, 2023.
7. Katzan, Cynthia M.; and Edwards, Jonathan L.: Lunar Dust Transport and Potential Interactions with Power System Components. Contractor Report, Sverdrup Technology, Inc., 1991.
8. Zeng, Xiangwu; He, Chunmei; Oravec, Heather; Wilkinson, Allen; Agui, Juan; and Asnani, Vivake: Geotechnical Properties of JSC-1A Lunar Soil Simulant. Journal of Aerospace Engineering, vol. 23 no. 2, 2009, pp. 111-116.
9. Jimenez, Nathan: Dusty Environment Classification and Testing: Dust Mitigation Slide Cleaning Material Study. Lunar Surface Innovation Consortium, Johns Hopkins Applied Physics Laboratory, 2022.
10. Jimenez, Nathan; and Gerdts, Stephen; Dusty Environment Classification & Testing. Game Changing Development Dust Mitigation Slide: Wipes and Tapes, 2022.
11. Gerdts, Stephen; Jimenez, Nathan; and Dunlap, Patrick H. Jr.: Uniform Dust Deposition System for Dust Tolerance Studies. ASCE Earth and Space, 2022.
12. National Aeronautics and Space Administration: Classifications and Requirements for Testing Systems and Hardware to be Exposed to Dust in Planetary Environments. NASA-STD-1008, 2021. https://ntrs.nasa.gov
13. Quick, Emma J.; Kurwitz, Cable; Hurlbert, Kathryn M.; and Suess, Leonard E.: Determination of Percent Area Coverage of Lunar Simulant on a Surface and Observations of Fairy Castle Structures. ASCEND, AIAA Aviation Forum, 2024.
14. Litofsky, Joshua H.; Nagpal, Sonali R.; and Michael, Hull W.: Demonstration of Portable X-ray Fluorescence Spectroscopy for High-Throughput In-Situ Quantification of Surface Lunar Dust for Testing and Future Surface Missions. NASA/TM-20240012216, 2024. https://ntrs.nasa.gov
15. Dijkstra, Edsger W.: A Note on Two Problems in Connexion with Graphs. Numerische Mathematik, 1959.